INDUCTION HEATING OF CIRCULAR FERROMAGNETIC PLATES

by

WILLIAM GERARD HURLEY

B.E. (Elect.), University College Cork, Eire
(1974)

SUBMITTED IN PARTIAL FULFILLMENT OF THE

REQUIREMENTS FOR THE DEGREE OF

MASTER OF SCIENCE

at the

MASSACHUSETTS INSTITUTE OF TECHNOLOGY

December, 1975
(i.e. February 1976)

Signature of Author.
    Department of Electrical Engineering and Computer Science,
                                         December 19, 1975

Certified by.
                                         ....
                                        Thesis Supervisor

Accepted by.
                                         ....
        Chairman, Departmental Committee on Graduate Students

INDUCTION HEATING OF CIRCULAR FERROMAGNETIC PLATES

by

WILLIAM GERARD HURLEY

Submitted to the Department of Electrical Engineering and Computer Science on December 19, 1975 in partial fulfillment of the requirements for the Degree of Master of Science.

ABSTRACT

Induction heating allows the generation of thermal energy in the heated element itself thereby eliminating the thermal contact resistance present in conventional heating methods. The induction heating of circular ferromagnetic plates is studied to predict power levels under various a.c. magnetic excitation conditions.

A lumped parameter transformer model is developed with the nonlinear equivalent disk resistance expressed as a function of the terminal variables in the system. The transformer model is effectively applied to predict operating efficiencies and particularly the frequency response of the system. A working model is built and tested to compare analytical and experimental data. Extensive experimental results are presented to justify the theoretical model.

THESIS SUPERVISOR: John G. Kassakian

TITLE: Assistant Professor of Electrical Engineering

ACKNOWLEDGEMENTS

4

TABLE OF CONTENTS

6

LIST OF FIGURES

LIST OF TABLES

LIST OF SYMBOLS

A Magnetic vector potential

a Primary coil radius

a_2 Secondary disk radius

a_c Primary coil conductor mean radius

B Amplitude of the total flux density at the disk surface

B_r Amplitude of the radial flux density at the disk surface

B_z Amplitude of the axial flux density at the disk surface

b Primary coil width

c Primary coil height

E Electric field intensity

f Magnetic field excitation frequency

H Magnetic field intensity

h Heat transfer coefficient

I_{eq} Equivalent disk current

I'_{eq} Equivalent disk current reflected in the primary

I_m Magnetizing current in the transformer model

I_p Terminal current in the primary coil

J_n Bessel function of order n

J_s Eddy-current density at the disk surface

L Primary coil conductor length

L_ℓ Leakage inductance in the transformer model

L_m Magnetizing inductance in the transformer model

L_s Self inductance of the primary coil

M Mutual inductance

N Number of turns in the primary coil

$P_{a.c.}$ A.C. power input to the induction system without a current-sampling resistor

P_{CD} Power input to the coil and disk

P_E Effective heating rate in the boiling test

P_{in} A.C. power input to the induction system with a current-sampling resistor

R_C Primary coil conductor resistance

R_D Equivalent disk resistance

R_R Equivalent disk resistance reflected in the primary

r Radius

T Temperature

t Time

V_p Terminal voltage in the primary coil

X_ℓ Leakage reactance in the transformer model

X_m Magnetizing reactance in the transformer model

Δ Primary coil conductor thickness

δ Skin depth

η_o Overall induction system efficiency

η_{CD} Coil-disk efficiency

θ Phase angle

μ Permeability

μ_o Permeability of free-space $4\pi \times 10^{-7}$ H/m

μ_r Relative permeability

ρ Radius

σ Electrical conductivity

ω Magnetic field excitation frequency

CHAPTER 1

INTRODUCTION

Heating methods without thermal contacts are based on the phenomenon of electromagnetic induction. A.C. current is produced in a conductor when placed in an alternating magnetic field which gives rise to a heating effect within the conductor. This concept has been successfully exploited in metallurgical processes for localized and high-speed through-heating of various articles. These characteristics of induction heating can be applied effectively to the development of the induction range.

The basic arrangement for an induction range is that shown in Figure 1.1(a) in which an alternating magnetic field is produced by an exciting coil which in turn induces eddy-currents in a conducting circular plate placed above the coil. As a consequence of the magnetic coupling between the primary coil and secondary metallic body, eddy-currents flow in circular paths giving rise to a heating effect and also a body force acting on the disk as a result of the interaction between the eddy-currents and radial magnetic field. To carry out a theoretical study of the system a lumped-parameter transformer model is developed as shown in Figure 1.1(b).

Induction heating allows the generation of thermal energy in the cooking vessel itself, thereby eliminating the thermal contact resistance between the heating element and the cooking vessel in a conventional range. This causes the heating element to have a much higher temperature than the vessel particularly when rough surfaces are present. An inductively heated vessel would reduce the thermal inertia of the overall
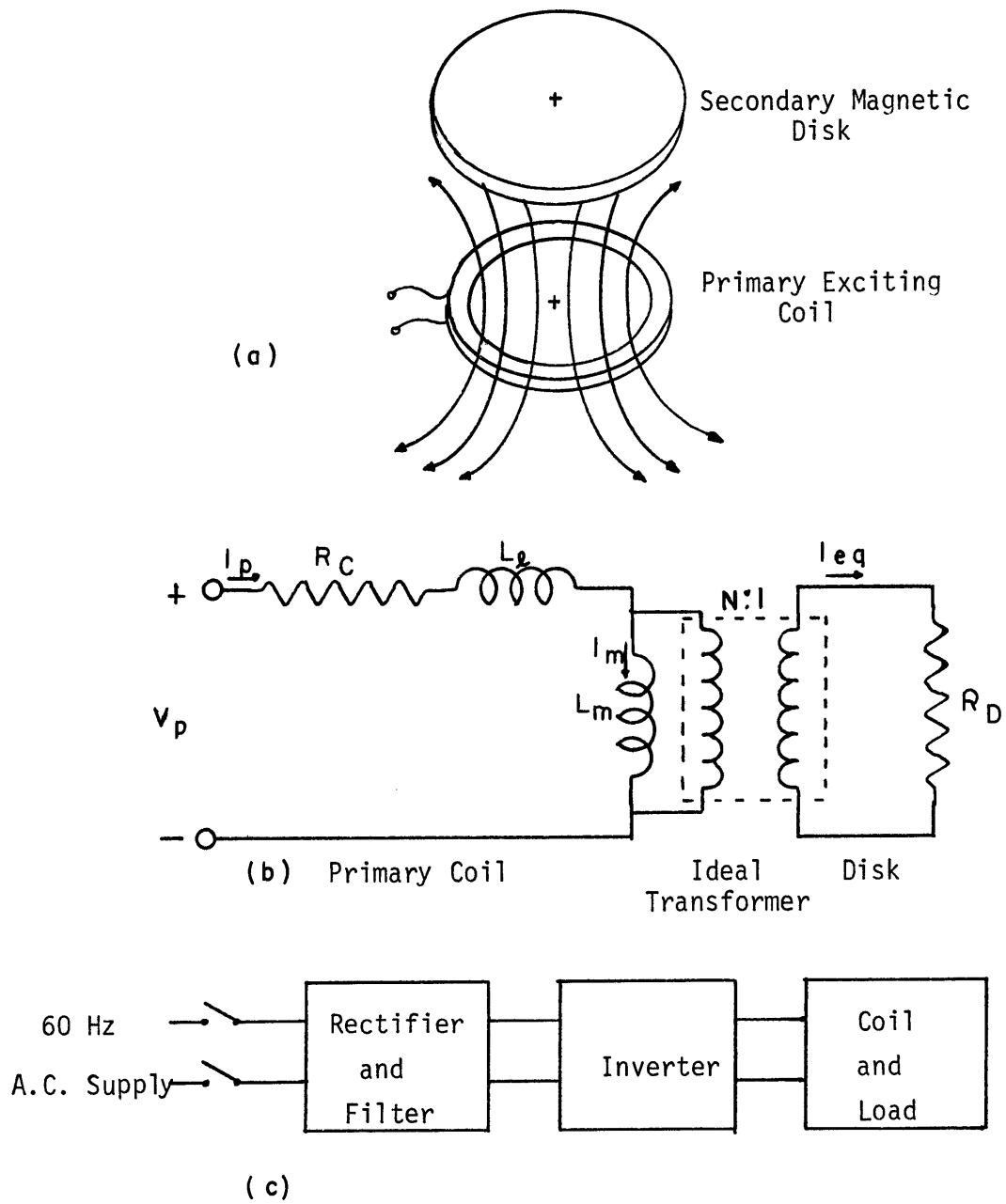
Figure 1.1: (a) Coil and Disk Arrangement

(b) Lumped Parameter Model

(c) Block Diagram of the Induction System

system allowing faster control of the operating temperatures. This would reduce much of the energy dissipated in conventional ranges after the power has been switched off while at the same time reducing air-conditioning requirements in confined spaces. As a result of lower cook-top temperatures safety is enhanced. Maintenance would be facilitated by the construction in modules. The effects of electromagnetic radiation emanating from an induction system have been studied and no harmful effects have been detected.[1,2] However, many technical problems exist with the successful development of the induction range, this thesis undertakes a study of these problems and implements proposed methods of solution.

Maxwell's Equations may be solved using the magnetic vector potential to give the magnetic field distribution around a current-carrying coil. Using the principle of superposition two concentric coils with an axial separation may be considered and the mutual inductance derived. In the coil-disk arrangement of Figure 1.1(a) the disk can be decomposed into circular filaments and the above results used to find the mutual inductance between the primary coil and each filament and also between filaments of the disk. By superposition the inductance terms in the transformer model may be found, Figure 1.1(b).

In order to create practical power levels it is necessary to use a circular ferromagnetic plate. Because of its non-linear permeability the modeling of the disk resistance becomes a difficult problem, since its value behaves as a function of the current flowing in the primary coil. As a result of the eddy-currents the magnetic field in the disk decays exponentially from the surface. This decay is characterized by the skin depth of the magnetic material. The eddy-current density has

a similar decay but using the Poynting Vector it is possible to take the decomposed disk and characterize each circular segment with an equivalent current and resistance and thus reducing the problem to that of a current-carrying coil. However, the equivalent current and resistance of each filament is a function of the non-linear permeability. If each filament is characterized by its own permeability obtained from an experimentally determined magnetization curve for the material, then superposition can be used to determine the power generated in the disk and the equivalent resistance, R_D, of the disk. The resistance of the primary coil can be determined from the conductor properties and corrections made for high frequency operation. Using the complete parameter model the effects of frequency of excitation and current levels in the primary are studied for efficiency of operation.

The studies carried out using the lumped parameter model suggest that high frequency operation is desirable from the point of view of power levels and efficiency. Operation above 20 kHz eliminates the problem of acoustic noise. However, the cost per watt increases rapidly with frequency. The system constructed operates at 10 kHz where acceptable power levels and efficiency are obtained at a reasonable cost. Two induction ranges already built[1,3] operated at 22 kHz and 35 kHz.

In previous designs a major problem arose with the dissipation of the energy due to copper losses in the primary coil. The hitherto solution has been to use forced convection cooling by placing a fan beneath the coil and allowing air to flow through the center of the coil and between the top of the coil and range surface. There are two major

disadvantages with this scheme. Firstly, the levels of flow required,
meant "noisy" systems which offset the elimination of acoustic noise by
high frequency operation. Secondly, for such a system to operate a
clearance must exist between the coil and range surface, this is un-
desirable because the power generated in the disk falls off rapidly with
increasing axial separation due to the reduction in magnetizing flux
(L_m in the lumped parameter model). In the system studied here,
advantage is taken of skin depth by using a hollow conductor for the
exciting coil and removing heat by forced convection with fluid flow
through the hollow conductor. Not only does this mean a quieter system
but it enhances the coupling between the primary and secondary by
eliminating the clearance space. This allows a lower operating frequency
for the same magneto-motive force and power level requirements.

A block diagram of the complete induction system is shown in
Figure 1.1(c). Power is fed from the A.C. supply (60 Hz) to a rectifier
and filter circuit, the D.C. output is used to drive a 10 kHz inverter
circuit with a sinusoidal output supplied to the primary coil at the
working frequency. The lumped parameter model facilitates the design
and choice of system components since the inverter output voltage and
current are fixed by the coil and disk. A digital trigger circuit
is designed to pulse the SCR's such that the triggering of two thyristors
simultaneously resulting in a short circuit of the inverter is
eliminated.

CHAPTER 2

DEVELOPMENT OF THE TRANSFORMER MODEL

2.1 Field Theory Solution of the Electromagnetic Field

For a magnetoquasistatic system[4], the following forms of Maxwell's

equations hold in a linear homogenious isotropic medium

$$\nabla \times \bar{H} = \bar{J}_f \tag{2.1.1}$$

$$\nabla \cdot \bar{B} = 0 \tag{2.1.2}$$

$$\nabla \cdot \bar{J}_f = 0 \tag{2.1.3}$$

$$\nabla \times \bar{E} = - \frac{\partial \bar{B}}{\partial t} \tag{2.1.4}$$

$$\bar{B} = \mu_0(\bar{H} + \bar{M}) \tag{2.1.5}$$

$$= \mu\bar{H} \tag{2.1.6}$$

$$\bar{B} = \nabla \times \bar{A} \tag{2.1.7}$$

$$\nabla \cdot \bar{A} = 0 \tag{2.1.8}$$

Combining (2.1.1), (2.1.6), (2.1.7) and (2.1.8) we obtain

$$\nabla^2\bar{A} = - \mu\bar{J}_f \tag{2.1.9}$$

A is the magnetic vector potential and in the case of cylindrical

symmetry where only the angular component exists (2.1.9) may be expanded

to give

$$\nabla^2 A_\phi = \frac{1}{r} \frac{\partial}{\partial r} \left(r \frac{\partial A_\phi}{\partial r} \right) + \frac{\partial^2 A_\phi}{\partial z^2} - \frac{A_\phi}{r^2} = - \mu J_f \tag{2.1.10}$$

If the current density J_f = 0, we obtain

$$\frac{1}{r} \frac{\partial}{\partial r} \left(r \frac{\partial A_\phi}{\partial r} \right) + \frac{\partial^2 A}{\partial z^2} - \frac{A_\phi}{r^2} = 0 \tag{2.1.11}$$

for which we may assume a solution of the form

$$A_\phi = R(r) \cdot Z(z) \qquad\qquad (2.1.12)$$

where R is a function of r only and Z a function of z only, equation (2.1.11) becomes

$$\frac{1}{Rr} \frac{\partial}{\partial r} \left(r \frac{\partial R}{\partial r} \right) - \frac{1}{r^2} = - \frac{1}{Z} \frac{\partial^2 Z^2}{\partial z^2} \qquad\qquad (2.1.13)$$

The left hand side of (2.1.13) is a function of z only and since R and Z are independent then there exists a k such that

$$- \frac{1}{Z} \frac{\partial^2 Z}{\partial z^2} = - k^2 \qquad\qquad (2.1.14)$$

Now equations (2.1.13) and (2.1.14) may be written in the form

$$r \frac{\partial}{\partial r} \left(r \frac{\partial R}{\partial r} \right) + (k^2 r^2 - 1) \, R = 0 \qquad\qquad (2.1.15a)$$

$$\frac{d^2 Z}{dz^2} - k^2 Z = 0 \qquad\qquad (2.1.15b)$$

Equation (2.1.15b) has solutions

$$Z(z) = E_k \, e^k + F_k \, e^{-kz} \qquad k \neq 0 \qquad\qquad (2.1.16a)$$

$$= Ez + f \qquad\qquad k = 0 \qquad\qquad (2.1.16b)$$

Equation (2.1.15a) is the general Bessel Equation with n = 1 and so has a solution of the form[5]

$$R(r) = AJ_1(kr) + BN_1(kr) \quad k \neq 0 \qquad\qquad (2.1.17a)$$

$$= Ar + B \frac{1}{r} \qquad\qquad k = 0 \qquad\qquad (2.1.17b)$$

E, F, A, B are constants determined from boundary conditions, n, k are real.

$J_1(kr)$ is the Bessel Function of order 1 and argument kr.

$N_1(kr)$ is the Neumann Function of order 1 and argument kr.

Note that the above solution only applies for the current density

$J_f = 0$.

Consider now a coil carrying a current i in a single plane loop of radius a as shown in Figure 2.1 where the plane of the coil defines z = 0. This is a case of cylindrical symmetry where the vector potential has an angular component only so the solution derived above applies. We divide the solution into two parts, that above the plane of the coil (z > 0) and that below it, in these regions $J_f = 0$ only if the conductivity σ is zero ($\bar{J}_f = σ\bar{E}$).

In equation (2.1.17) B is zero since a finite solution exists at r = 0 and the Neumann function $N_1(r)$ has a singularity at the origin. Thus combining (2.1.16) and (2.1.17) in (2.1.12) we obtain

$$A_\phi^+ = \int_0^\infty A^+(k) \, J_1(kr) \, e^{-kz} \, dk \qquad z > 0$$

$$A_\phi^- = \int_0^\infty A^-(k) \, J_1(kr) \, e^{kz} \, dk \qquad z < 0$$

(2.1.18)

Here the solution is in integral form since k is a continuous eigenvalue.[6]

Equations (2.1.1) and (2.1.2) impose two boundary conditions at the coil plane z = 0.

The first implies

$$n \times (\bar{H}^+ - \bar{H}^-) = \bar{k}_f \qquad (2.1.19)$$

where n is the normal vector to the coil plane and $\bar{k}_f$ is the surface current density at the boundary which in this case is given by

$$\bar{k}_f = \bar{i} \, δ \, (r - a) \qquad (2.1.20)$$
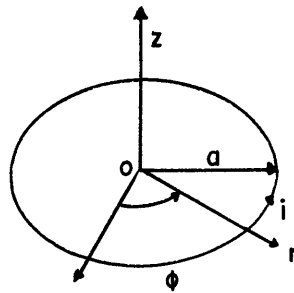
Figure 2.1   Single Loop Plane Coil Carrying Current i
Showing Co-ordinate System
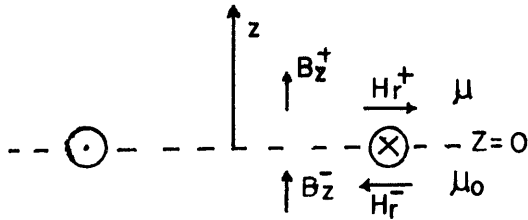
Figure 2.2   Conditions at the Boundary of Two Media
Characterized by Different Permeabilities

$\delta(r-a)$ is the Dirac-delta function.

From (2.1.6) and (2.1.7) we obtain

$$H_r = -\frac{1}{\mu} \frac{\partial A_\phi}{\partial z} \qquad (2.1.21)$$

The second boundary condition arising from (2.1.2), i.e. $\nabla \cdot \bar{B} = 0$ implies $A_\phi^+ = A_\phi^-$ at $z = 0$ so that

$$A^+(k) = A^-(k) \qquad (2.1.22)$$

We shall now consider two cases, in the first we assume the coil is in free space i.e. characterized by a permeability μ_0 and conductivity $\sigma = 0$. In the second case we consider a medium in which the region above the coil ($z > 0$) is characterized by a permeability μ and the region below ($z < 0$) by that of free space μ_0. In this case we again assume the total medium is characterized by zero conductivity to ensure that the current density J_f is zero for the derived solution to apply and so current is confined only to the coil creating the field. The necessity for this refinement will become apparent later when in a physical system the magnetic medium will have a finite conductivity.

Case One

Here the total medium has a permeability μ_0 and zero conductivity.

Applying the first boundary condition (2.1.19) to (2.1.18) using (2.1.20) and (2.1.21) we have

$$\frac{1}{\mu_0} \left| \int_0^\infty A^+(k)J_1(kr)e^{-kz}k\,dk + \int_0^\infty A^-(k)J_1(kr)e^{kz}k\,dk \right|_{z=0} = i\delta(r-a) \qquad (2.1.23)$$

Evaluating and rewriting using k' instead of k we obtain

$$\frac{1}{\mu_0} \int_0^\infty \left[A^+(k') + A^-(k') \right] J_1(k'r)k'\,dk' = i\delta(r-a) \qquad (2.1.24)$$

Now multiply both sides by $J_1(kr)r$ and integrate from $r = 0$ to $r = \infty$

$$\int_0^\infty J_1(kr)rdr \int_0^\infty \left[A^+(k') + A^-(k')\right] J_1(k'r)k'dk'$$

$$= \mu_0 \int_0^\infty i\delta(r-a)J_1(kr)rdr \tag{2.1.25}$$

From the Fourier Bessel Integral[6]

$$f(k) = \int_0^\infty J_m(kr)rdr \int_0^\infty f(k')J_m(k'r)k'dk' \tag{2.1.26}$$

We also have from the properties of the Dirac-delta function

$$\int_0^\infty i\delta(r-a)J_1(kr)rdr = iJ_1(ka)a \tag{2.1.27}$$

Substituting these two results in (2.1.25) we obtain

$$A^+(k) + A^-(k) = \mu_0 \ i \ a \ J_1(ka) \tag{2.1.28}$$

Combining this with the second boundary condition (2.1.22) the complete solution for (2.1.18) for case one is

$$A_\phi^{\pm}(r,z) = \frac{\mu_0 ia}{2} \int_0^\infty J_1(ka)J_1(kr) \ e^{\mp kz} \ dk \tag{2.1.29}$$

Case Two

In this case the region $z > 0$ is characterized by a permeability μ while the region $z < 0$ is characterized by μ_0. Both regions have zero conductivity. Figure 2.2 illustrates the two regions as well as the conditions at the boundary.

As in case one we apply the first boundary condition (2.1.19) to (2.1.18) using (2.1.20) and (2.1.21) now taking account of the different permeabilities to obtain

$$\frac{1}{\mu} \left[\int_0^\infty A^+(k)J_1(kr)e^{-kz}k\,dk \right] + \frac{1}{\mu_0} \left[\int_0^\infty A^-(k)J_1(kr)e^{kz}k\,dk \right] = i\delta(r-a)$$

$$(2.1.30)$$

Proceeding with the solution as before using the Fourier Bessel Integral we obtain

$$\frac{1}{\mu} A^+(k) + \frac{1}{\mu_0} A^-(k) = iaJ_1(ka) \qquad (2.1.31)$$

The same boundary condition on the magnetic flux density applies so that $A^+(k) = A^-(k)$ and

$$A^+(k) = \frac{\mu_0}{1 + \dfrac{\mu_0}{\mu}} aiJ_1(ka) \qquad (2.1.32)$$

For a ferro-magnetic material $\mu \gg \mu_0$ so

$$A^+(k) \simeq \mu_0 \, aiJ_1(ka) \qquad (2.1.33)$$

This is a factor of 2 greater than that obtained for case one with a non-magnetic medium. Thus in this case the complete solution for A_ϕ is

$$A_\phi^{\pm}(r,z) = \mu_0 \, ai \int_0^\infty J_1(ka)J_1(kr)e^{\mp kz} \, dk \qquad (2.1.34)$$

2.2 Eddy-Current Density Distribution in the Disk

The basic arrangement for an induction heating system is shown in Figure 2.3 where the alternating magnetic field is produced by an exciting primary coil which produces eddy currents in the disk. As stated in the introduction the magnetic coupling between the primary coil and secondary conducting body, characterized by a permeability μ and conductivity σ, gives rise to eddy-currents which flow in coaxial circular paths and produce secondary vector potential fields. The eddy currents will be in the opposite direction to that of the primary coil
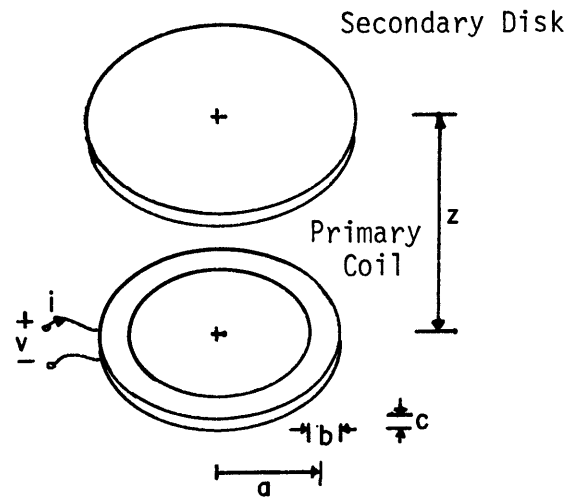
Figure 2.3 Coil and Disk Arrangement in an Induction
Heating System
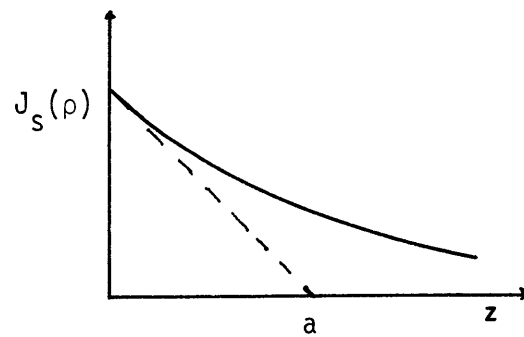
Figure 2.4 Axial Decay of Eddy Current Density in a
Disk Placed in an Alternating Magnetic
Field.

current. The solutions we have already derived for the vector potential field due to a current carrying coil will apply here for the primary coil. If we now decompose the secondary disk into circular filaments carrying eddy currents then the derived solutions also apply provided we can satisfy the conditions under which those solutions hold. By superimposing the two solutions we can find the total vector potential and from this the eddy current density distribution and the flux density distribution. Since the vector potential has angular components only then they may be added algebraically. To simplify the solution of the governing integral equations we shall assume in the analysis that follows that the disk is infinite in the radial direction and semi-infinite in the axial direction. In practice these assumptions are reasonable to predict the quantities of interest such as power absorbed and equivalent resistance provided the disk radius is greater than 1.5 times that of the primary coil radius and that the skin depth of the disk is less than one fifth of the disk thickness.

The two properties of interest in the disk are its magnetic permeability and electrical conductivity σ. The permeability μ is a non linear function of the flux level, however, if we assign permeabilities in accordance with flux levels in each filament of the decomposed disk then we can apply the principle of superposition. The solutions for the magnetic vector potential in equation (2.1.18) assume the coil to be placed in a medium of zero conductivity and later we distinguished between magnetic and non-magnetic media but still assuming no conductivity. To account for the finite disk conductivity we shall assume the coil is situated in a medium with one region having a

permeability μ (case two) and utilizing the Poynting Vector reduce
the eddy currents in the disk to equivalent currents flowing in a thick-
ness δ, the skin depth in the disk and then apply case two to the
equivalent currents.

Applying case two to the coil neglects the coil-disk separation,
which is reasonable provided there is close coupling as would be the
case in a physical system. From equation (2.1.34) for an N turn primary
carrying a magnetizing current of complex amplitude $\hat{I}_m$ then the complex
amplitude of the vector potential is

$$\hat{A}_s(r,z) = \mu_0 N \hat{I}_m a \int_0^\infty J_1(ka)J_1(kr)e^{-kz}dk \qquad (2.2.1)$$

Equation (2.2.1) assumes all the turns are concentrated at a radius a.
We drop the suffix ϕ since we are interested in the angular component
only. We will write A_s for $\hat{A}_s$ etc. By considering Maxwell's Equations
it can be easily shown that the eddy-currents and magnetic flux density
decay exponentially into the disk where the decay is characterized by
the skin depth δ as shown in Figure 2.4, where $J_s(\rho)$ is the complex
amplitude of the eddy-current density at the surface of the disk and
radius ρ. The skin depth δ is given by the formula

$$\delta = \sqrt{\frac{2}{\omega\mu_0\sigma}} \qquad (2.2.2)$$

where ω is the exciting frequency. Further consideration of the Poynting
Vector at the disk surface shows that an equivalent rms current
$J_s(\rho)/2$ δdρ flowing in an annular segment of width dρ and thickness δ
at a radius ρ gives rise to the same absorbed power in the disk [an
extensive discussion on the concept of equivalent current for eddy

currents is given by Ryder, reference [7] pages (437-442)].

Since we have already assumed that disk to be semi-infinite in the axial direction, which is justified by assuming disks where the skin depth is a factor of five less than the disk thickness, then case two applies to the eddy currents. The amplitude of the vector potential at the disk surface due to the equivalent current in an annular segment at a radius ρ is, from (2.1.34)

$$dA_e(r,z) = \mu_0 \; \rho \; \sqrt{2} \; \frac{J_s(\rho)}{2} \; \delta d\rho \int_0^\infty J_1(k\rho)J_1(kr)dk \qquad (2.2.3)$$

Equation (2.1.34) is evaluated for $z = 0$. The amplitude of the equivalent current in a segment is $\sqrt{2} \; x \; \dfrac{J_s(\rho)}{2}$. Since we are interested in the conditions at the disk surface, the origin of z is now taken at the plane of the primary coil and interpreted as the coil disk separation. Thus $dA_e(r,z)$ is the vector potential at the disk surface, a distance z from the primary coil, at a radius r due to eddy-currents in a segment at a radius ρ in the disk.

Combining (2.2.1) and (2.2.3) using the principle of superposition the complex amplitude of the angular component of the magnetic vector potential at the disk surface due to the primary coil current and disk eddy-currents is

$$A(r,z) = \mu_0 NI_m a \int_0^\infty J_1(ka)J_1(kr)e^{-kz}dk$$

$$+ \frac{\mu_0 \delta}{\sqrt{2}} \int_0^\infty J_s(\rho)\rho d\rho \int_0^\infty J_1(k\rho)J_1(kr)dk \qquad (2.2.4)$$

Also combining (2.1.4) and (2.1.7) we have

$$\nabla \times \bar{E} = - \nabla \times \frac{\partial \bar{A}}{\partial t} \qquad (2.2.5)$$

Also

$$\bar{J}_f = \sigma \bar{E} \tag{2.2.6}$$

$$= - \sigma \frac{\partial \bar{A}}{\partial t}$$

Now for

$$A(r,z,t) = A(r,z)e^{j\omega t} \tag{2.2.7}$$

then

$$J_s(r,z) = - j\omega\sigma A(r,z) \tag{2.2.8}$$

Where $A(r,z)$ is given by (2.2.4) thus

$$J_s(r,z) = - j\omega\mu_0\sigma \{ NI_m a \int_0^\infty J_1(ka)J_1(kr)e^{-kz} \, dk$$

$$+ \frac{\delta}{\sqrt{2}} \int_0^\infty J_s(\rho)\rho d\rho \int_0^\infty J_1(k\rho)J_1(kr)dk\} \tag{2.2.9}$$

We now solve for $J_s(r)$ at the disk surface using the Fourier-Bessel Integral. We drop z from $J_s(r,z)$ since z is interpreted as the coil-disk separation. Multiply both sides of (2.2.9) by $J_1(kr)rdr$ and inegrate from $r = 0$ to $r = \infty$. Using the Fourier-Bessel Integral (2.2.26) the right-hand side of equation (2.2.9) can be manipulated as follows

$$\int_0^\infty J_1(kr)rdr \int_0^\infty \{ \frac{1}{k'} J_1(k'a)e^{-k'z} \} J_1(k'r)k'dk'$$

$$= \frac{1}{k} J_1(ka)e^{-kz} \tag{2.2.10}$$

$$\int_0^\infty J_1(kr)rdr \int_0^\infty \{ \frac{1}{k'} \int_0^\infty J_s(\rho)J_1(k'\rho)\rho d\rho \} J_1(k'r)k'dk'$$

$$= \frac{1}{k} \int_0^\infty J_s(\rho)J_1(k\rho)\rho d\rho$$

$$= \frac{1}{k} \int_0^\infty J_s(r) J_1(kr) r dr \qquad (2.2.11)$$

Now equation (2.2.9) becomes

$$\int_0^\infty J_s(r) J_1(kr) r dr = - j\omega\mu_0 \sigma NI_m \frac{1}{k} J_1(ka) e^{-kz}$$

$$- \frac{j\omega\mu_0 \sigma\delta}{\sqrt{2}} \frac{1}{k} \int_0^\infty J_s(r) J_1(kr) r dr \qquad (2.2.12)$$

Rearranging (2.2.12) we obtain

$$\int_0^\infty J_s(r) J_1(kr) r dr = \frac{-j\omega\mu_0 \sigma NI_m a}{k[1 + \dfrac{j\omega\mu_0 \sigma\delta}{\sqrt{2} k}]} J_1(ka) e^{-kz} \qquad (2.2.13)$$

Again multiply both sides by $J_1(kr) k dk$ and integrate from $k = 0$ to

$k = \infty$ and simplify using the Fourier-Bessel Integral (2.1.26)

$$J_s(r) = \int_0^\infty J_1(kr) k dk \int_0^\infty J_s(r') J_1(kr') r' dr' \qquad (2.2.14)$$

$$J_s(r) = - j\omega\mu_0 \sigma NI_m a \int_0^\infty \frac{J_1(ka) J_1(kr) e^{-kz}}{[1 + \dfrac{j\omega\mu_0 \sigma\delta}{\sqrt{2} k}]} dk \qquad (2.2.15)$$

This is the final expression for the complex amplitude of the eddy

current density at the surface of a disk at a radius r and a distance

z above the plane of a coil carrying a magnetizing current of

amplitude I_m.

2.3 Magnetic Flux Density Distribution in the Disk

Mathematically it is not strictly correct to use a field dependent

non-linear permeability in a linear theory. However using the segment

approach, where each annular segment is assigned its own characteristic

permeability and then carrying out integration over all the segments does

approach the true solution. The mathematical derivation of the current density distribution at the disk surface included μ, in the form of δ the skin depth, as a function of the variable of integration r in (2.2.15), we shall see later that the formulae for the power dissipated in the disk and the disk equivalent resistance also incorporate this dependence of μ on the variable of integration. Only if this dependence is strictly adhered to can the principle of superposition of linear system theory be applied. To determine the characteristic permeability of each segment we must first calculate the flux density distribution in the disk.

Combining equations (2.1.4) and (2.2.6) we have

$$\frac{\partial \bar{B}}{\partial t} = -\frac{1}{\sigma} (\nabla \times \bar{J}_s) \tag{2.3.1}$$

Since the eddy current density has an angular component only then the complex amplitudes of the axial and radial components of the magnetic flux density at the disk surface are given by

$$Bz = -\frac{1}{j\omega\sigma} (\frac{\partial J_\phi}{\partial r} + \frac{J_\phi}{r}) \tag{2.3.2}$$

$$Br = -\frac{1}{j\omega\sigma} (-\frac{\partial J_\phi}{\partial z}) \tag{2.3.3}$$

where J_ϕ is the angular component of eddy current at the disk surface i.e. $J_s(r,z)$.

Substituting (2.2.15) into (2.3.2) noting the relation[*] we obtain

---

[*] $\frac{d}{dx} J_n(x) = J_{n-1}(x) - \frac{n}{x} J_n(x)$

$$B_z(r) = \mu_0 NI_m a \int_0^\infty \frac{J_1(ka)J_0(ka)e^{-kz} k}{[1 + \dfrac{j\omega\mu_0\sigma\delta}{\sqrt{2}\ k}]} dk \qquad (2.3.4)$$

$$B_r(r) = \mu_0 NI_m a \int_0^\infty \frac{J_1(ka)J_1(kr)e^{-kz}k}{[1 + \dfrac{j\omega\mu_0\sigma\delta}{\sqrt{2}\ k}]} dk \qquad (2.3.5)$$

To find the total flux density at a radius r we take the vector sum of the complex amplitudes of the axial and radial components

$$B(r) = B_r(r) + jB_z(r) \qquad (2.3.6)$$

Using the amplitude of this the distribution $\mu(r)$ of the permeability is found from the normalized magnetization curve for the disk material.

B(r) gives the radial distribution of flux at the disk surface. The axial variation of flux density follows the same exponential decay as the eddy-current density Figure 2.4. A further refinement could be made on the permeability due to the axial variation of flux. However we are mainly interested in the equivalent skin depth region where the power is absorbed. As a first approximation we could define an equivalent flux corresponding to the equivalent current (section 2.2) having an equivalent rms value 1/2 B(r) where B(r) is the complex amplitude at the surface. The amplitude of the equivalent flux density would be $1/\sqrt{2}$ B(r) or 0.707 B(r). We shall see later on the magnetization curve for cold rolled steel that over wide ranges of flux the permeability μ remains essentially constant. Thus refining μ using 0.707 B(r) instead of B(r) is rendered meaningless by the small change in μ and also by the errors accumulated in experimental data and numerical integration.

Note also $\delta \propto \dfrac{1}{\sqrt{\mu}}$ which is the quantity of interest.

2.4 Transformer Model Parameters

With the current and flux distributions derived in sections (2.2) and (2.3) we are in a position to derive expressions for the parameters of the transformer model in terms of these distributions. In deriving the expressions we made two assumptions, i.e. the disk is infinite in its radial dimension and semi-infinite in the axial direction. The latter assumption allows the use of the Pounting Vector to form an equivalent secondary disk current flowing in an equivalent resistance, the lumped parameter secondary disk resitance R_D. The resistance of the primary coil R_C, can be calculated from the physical dimensions and electrical properties of the coil conductor with corrections made for high frequencies where skin depth phenomena are prominent. The inductance terms can be found from the flux distribution by dividing the disk into annular segments and setting up inductance matrices to represent the mutual inductance of the segments and from these the magnetizing and leakage inductance terms are found.

(a) Disk Resistance R_D

For an annular segment at a radius r of width dr then from the Poynting Vector[7] we can find the equivalent rms current as in equation (2.2.3) which is

$$dI = \frac{J_s(r)}{2} \, \delta dr \qquad\qquad (2.4.1)$$

where $J_s(r)$ is the amplitude of the eddy current density at the disk surface given by (2.2.15).

This equivalent current flows in a thickness δ, the skin depth, so the equivalent resistnce of the segment is

$$dR = \frac{2\pi r}{\sigma \delta dr} \tag{2.4.2}$$

where δ which is a function of μ (equation 2.2.2) is evaluated at the radius r, σ is the disk conductivity.

The average power flowing into the segment is then given by

$$dP = [dI_{eq}]^2 dR$$

$$= \frac{\pi}{2\sigma} [J_s(r)]^2 \delta r dr \tag{2.4.3}$$

Integrating equations (2.4.1) and (2.4.3) over the whole disk we obtain

$$I_{eq} = \int_0^\infty \frac{J_s(r)}{2} \delta dr \tag{2.4.4}$$

$$P_D = \frac{\pi}{2\sigma} \int_0^\infty [J_s(r)]^2 \ \delta r dR \tag{2.4.5}$$

and the equivalent resistance of the disk is

$$P_D = \frac{P}{[I_{eq}]^2} \tag{2.4.6}$$

(b) Coil Resistance R_C

Since we are using a hollow conductor to provide forced convection cooling we assume that at the operating frequencies the thickness of the conductor Δ is greater than the skin depth.

The d.c. resistance is

$$R_{C \ d.c.} = \frac{N2\pi a}{\sigma_c 2\pi a_c \Delta}$$

where a is the mean coil radius, a_c is the mean conductor radius and σ_c is the electrical conductivity of the conductor, N is the number of turns.

$$R_{C \text{ a.c.}} = \frac{N2\pi a}{\sigma_c 2\pi a_c \delta} \tag{2.4.8}$$

so

$$\frac{R_{C \text{ a.c.}}}{R_{C \text{ d.c.}}} = \frac{\Delta}{\delta} \tag{2.4.9}$$

(c) Coil Self-Inductance L_s

Many formulae are available for coil self-inductance a suitable formula for the present case is

$$L_s = \mu_0 N^2 a \left\{ \ln \frac{2}{\sqrt{C}} \left(1 + 3C - \frac{15}{4} C^2 + \ldots \right) - \left(2 + C - \frac{31}{8} C^2 + \ldots \right) \right\} \tag{2.4.10}$$

$$C = \frac{R}{16a^2}$$

$$R = 0.2235 \ (b + c')$$

R is the geometric mean distance of the coil cross-section, this equation is given in reference [8], b and c' are the dimensions of the coil cross-section, Figure 1.3(a).

(d) Magnetizing Inductance L_m

The self inductance of the primary coil is given by the sum of the magnetizing and leakage components

$$L_s = L_m + L_\ell \tag{2.4.11}$$

If L_2 is the secondary inductance then the mutual inductance is

$$M = \sqrt{L_m L_2} \tag{2.4.12}$$

the coupling co-efficient is unity since by definition L_m excludes the leakage flux L_ℓ. We may write

$$L_m = \frac{M^2}{L_2} \qquad\qquad\qquad (2.4.13)$$

To evaluate the magnetizing inductance L_m we divide the disk into

segments and find the mutual inductance between the primary coil and

each segment to form a mutual inductance matrix [M]. We also find the

self inductance of each secondary segment using (2.4.10) and also the

mutual inductance between the various segments of the disk to give the

secondary inductance matrix $[L_2]$ with the self inductance terms on the

main diagonal. Rewriting (2.4.13) in matrix form we have

$$L_m = [M]_T \, [L_2]^{-1} \, [M] \qquad\qquad (2.4.14)$$

From the definition of mutual inductance

$$M_{12} = \frac{\lambda_2}{I_1}$$

$$= \frac{N_2}{I_1} \int_0^A B_{z1}(r) 2\pi r dr \qquad\qquad (2.4.15)$$

We can easily drive formulae for mutual inductance terms in (2.4.14)

using the equation for flux density distribution in section (2.3). For

the disk segments $N_2 = 1$, A will be the radius of a particular segment.

(e) Leakage Inductance L_ℓ

From equation (2.4.11) we have

$$L_\ell = L_s - L_m$$

with L_s given by (2.4.10) and L_m by (2.4.14).

2.5 Terminal Variables and Efficiency

In the last section we derived expressions for each of the model

parameters in Figure 2.5(a). An expression was also found for the
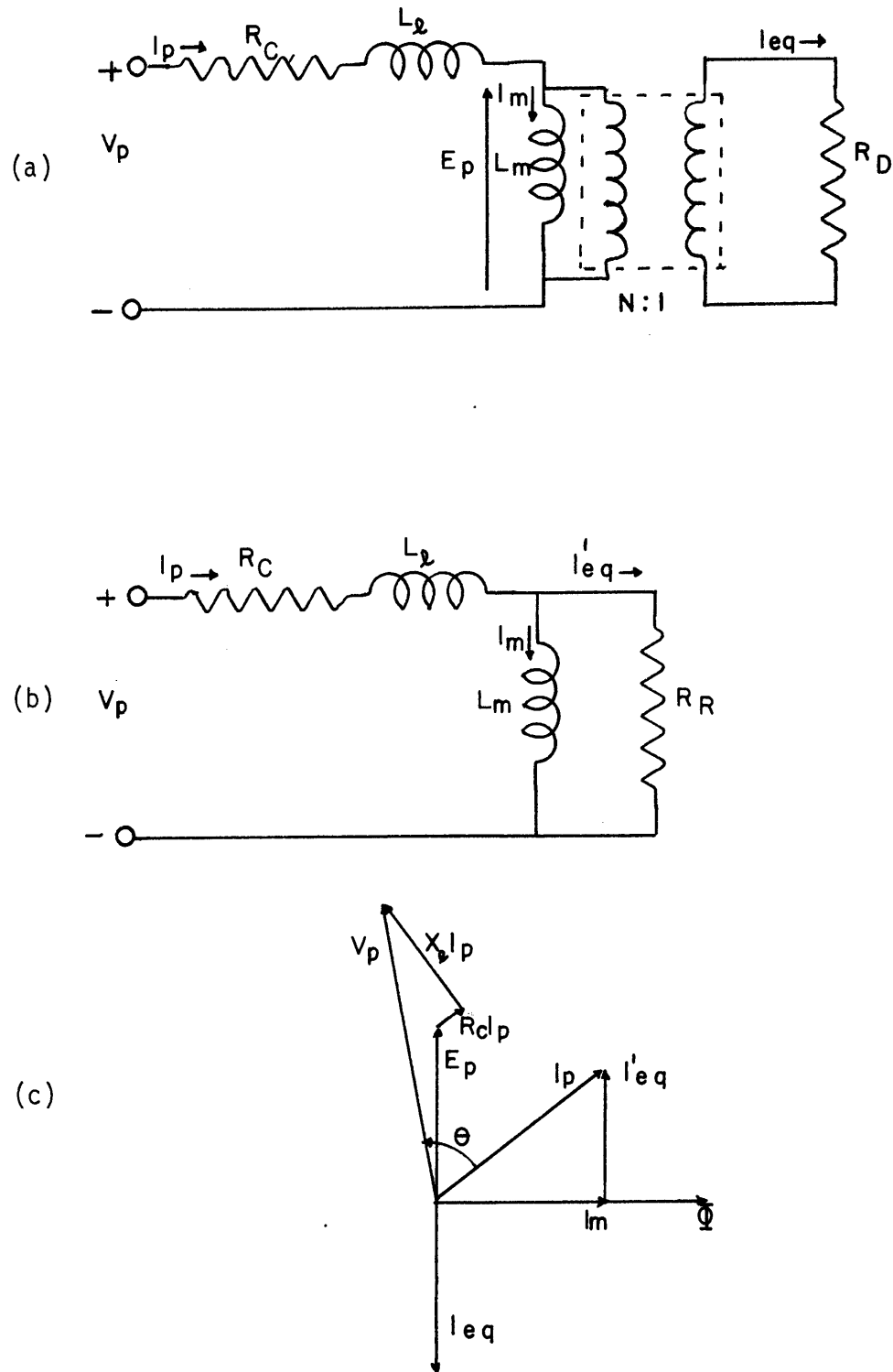
Figure 2.5 (a) Lumped Parameter Transformer Model

(b) Equivalent Circuit

(c) Phasor Diagram

equivalent load current I_{eq}. Both R_D and I_{eq} are functions of the current I_m flowing in the magnetizing branch of the model as expressed by equations (2.4.4) and (2.2.15), we reflect both of these quantities into the primary to give the equivalent circuit of Figure 2.5(b). With the aid of the equivalent circuit the phasor diagram of Figure 2.5(c) is set up from which the terminal voltage and current of the coil-disk arrangement are found.

The efficiency of the system can be found from the transformer model with knowledge of the various parameters. The current in the reflected resistance R_R from Figure 2.5(b) is

$$I_{eq}' = \left| \frac{jX_m}{R_R + jX_m} \right| \cdot I_P \qquad (2.5.1)$$

where X_m is the reactance of the magnetizing branch. The efficiency is

$$\eta_{CD} = \frac{P_{out}}{P_{in}}$$

$$= \frac{\left| \dfrac{jX_m}{R_R + jX_m} \right|^2 I_P{}^2 R_R}{R_C I_P{}^2 + \left| \dfrac{jX_m}{R_R + jX_m} \right|^2 I_P{}^2 R_R}$$

$$= \frac{\dfrac{R_R}{R_C}}{1 + \dfrac{R_R}{R_C} + \left(\dfrac{R_R}{X_m}\right)^2} \qquad (2.5.2)$$

CHAPTER 3

ANALYTICAL ANALYSIS AND DESIGN

3.1 The Non-Interaction Approximation

In Chapter 2 we derived expressions for all the quantities of interest in the transformer model. All the expressions involve either the current or flux density distributions (equations 2.2.15, 2.3.4, and 2.3.5), i.e.

$$J_s(r) = - j\omega\mu_0\sigma NI_m a \int_0^\infty \frac{J_1(ka)J_1(kr)e^{-kz}}{[1 + \frac{j\omega\mu_0\sigma\delta}{\sqrt{2}\,k}]} \cdot dk \qquad (2.2.15)$$

$$B_z(r) = \mu_0 NI_m a \int_0^\infty \frac{J_1(ka)J_0(kr)e^{-kz}}{[1 + \frac{j\omega\mu_0\sigma\delta}{\sqrt{2}\,k}]} k \cdot dk \qquad (2.3.4)$$

$$B_r(r) = \mu_0 NI_m a \int_0^\infty \frac{J_1(ka)J_1(kr)e^{-kz}}{[1 + \frac{j\omega\mu_0\sigma\delta}{\sqrt{2}\,k}]} k \cdot dk \qquad (2.3.5)$$

The denominator of the integrand is the same in all cases and evaluated with the properties of cold-rolled steel[*] at 10 kHz gives

$$1 + \frac{j\omega\mu_0\sigma\delta}{\sqrt{2}\,k} = 1 + 0.300/k \qquad (3.1.1)$$

Thus for large k the denominator approaches unity, while for small k the numerator approaches zero. Physically the denominator represents the effect of the eddy-currents in the disk in reducing the field.

---

[*]Cold-Rolled Steel: $\sigma = 6.7 \times 10^6$ $(\Omega m)^{-1}$; $\mu_r = 600$ (typical)

$\delta = 0.08$ mm = 3 mils at 10 kHz.

We derived the source field using case two i.e. with a magnetic half-plane and a consequent doubling of the source field. The presence of a separation between the coil and disk would reduce this factor. Actual measurements of inductance at 1 kHz show that the inductance increases from 92.5 μH to 94.0 μH or 1.6% with a magnetic disk of cold-rolled steel and 2 cm separation. The factor of two is reduced by the presence of the separation and the eddy currents in the disk.

Thus there are two opposing effects, on the one hand the field is augmented by the presence of the magnetic disk and on the other-hand reduced by the induced eddy-currents, the effects of the eddy-currents increasing with frequency (3.1.1). The overall effect must be to increase the field. On the basis of experimental observation it is reasonable to approximate the flux distributions as those due to the source alone and then derive the eddy-current distribution from this flux distribution using (2.2.8). Now case one applies and the magnetic field is from (2.1.7) and (2.1.29).

$$B_z(r) = \frac{\mu_0 NI_m a}{2} \int_0^\infty J_1(ka)J_0(kr)e^{-kz} \, k \, dk \tag{3.1.2}$$

$$B_r(r) = \frac{\mu_0 NI_m a}{2} \int_0^\infty J_1(ka)J_1(kr)e^{-kz} \, k \, dk \tag{3.1.3}$$

and from (2.2.8) and (2.1.29) we obtain

$$J_s(r) = - \frac{j\omega\mu_0\sigma NI_m a}{2} \int_0^\infty J_1(ka)J_1(kr)e^{-kz} dk \tag{3.1.4}$$

In the numerical analysis these expressions are used to determine the transformer model parameters as derived in sections (2.4) and (2.5).

We can interpret the approximation in terms of the transformer

model. In accordance with Lenz's Law the induced secondary ampere

turns tend to reduce the flux set up by the primary ampere turns.

However the magnetic circuit under no load is different from that

under load (case one and case two respectively) so that the increase

in flux due to the presence of the magnetic medium is offset by the

necessary reduction due to secondary ampere turns which in turn allows

the primary current to increase from I_m under no-load to I_p under full

load, Figure 2.5(c). Therefore the non-interaction approximation assumes

the magnetizing current I_m remains constant between no-load and full-

load thus maintaining the main flux (due to the source alone) constant

for both load conditions and that the magnetic affect of the secondary

current is neutralized by a corresponding component of the primary

current I_{eq}' as shown in Figure 2.5(c) for which

$$N_1 I_{eq}' = N_2 I_{eq} \qquad\qquad (3.1.5)$$

Here $N_1 = N$ the number of turns in the primary coil and $N_2 = 1$.

3.2 Numerical Solution of the Transformer Model Parameters

With the approximation introduced in section (2.1) we can reduce

all the quantitites of interest to the evaluation of two Bessel

Integrals for which convergent series are available[9]. As outlined in

the introduction the disk is divided into a given number of segments

and numerical integration then carried out over these segments.

The following series is available[9],

$$\int_0^\infty J_1(\mu) J_1(\lambda\mu) e^{-p\mu} \, d\mu$$

$$= \frac{1}{\pi\lambda^{1/2}} \left[\left(1 + 3C - \frac{15}{4} C^2 + \frac{35}{4} C^3 + \ldots \right)\ln \frac{2}{\sqrt{C}} - \left(2 + C - \frac{31}{8} C^2 \right. \right.$$

$$\left. \left. + \frac{247}{24} C^3 + \ldots \right) \right] \tag{3.2.1}$$

Where

$$C = \frac{P^2 + (1-\lambda)^2}{16\lambda}$$

Differentiating (3.2.1) with respect to P we obtain

$$\int_0^\infty J_1(\mu)J_1(\lambda\mu)e^{-p\mu}\mu d\mu$$

$$= \frac{P}{8\pi\lambda^{3/2}} \left[\left(-3 + \frac{15}{2} C - \frac{105}{4} C + \ldots \right)\ln \frac{2}{\sqrt{C}} + \left(\frac{1}{2C} + \frac{5}{2} - \frac{77}{8} C \right. \right.$$

$$\left. \left. + \frac{141}{4} C^2 + \ldots \right) \right] \tag{3.2.2}$$

The series converge for $p < 2$.

Using the substitutions

$$\mu = ka; \quad P = z/a, \quad \lambda = \frac{r}{a}, \quad C = \frac{z^2 + (a-r)}{16ar}$$

We obtain from the above analysis

$$BI1(r,a,z) = \int_0^\infty J_1(ka)J_1(kr)e^{-kz}dk$$

$$= \frac{1}{\pi\sqrt{ar}} \left[\left(1 + 3C - \frac{15}{4} C^2 + \frac{35}{4} C^3 + \ldots \right)\ln \frac{2}{\sqrt{C}} \right.$$

$$\left. - \left(2 + C - \frac{31}{8} C^2 + \frac{247}{24} C^3 + \ldots \right) \right] \tag{3.2.3}$$

and

$$BI2(r,a,z) = \int_0^\infty J_1(ka)J_1(kr)e^{-kz} kdk$$

$$= \frac{z}{8\pi(ar)^{3/2}} \left[(-3 + \frac{15}{2} C - \frac{105}{4} C^2 + \ldots) \ln \frac{2}{\sqrt{C}} \right.$$

$$\left. + (\frac{1}{2C} + \frac{5}{2} - \frac{77}{8} C + \frac{141}{4} C + \ldots) \right] \tag{3.2.4}$$

Finally we want an expression for the integral

$$BI3(r,a,z) = \int_0^\infty J_1(ka) J_0(kr) e^{-kz} \, k \, dk$$

We can reduce the integral to that of BI1 by integrating BI3 between

r and r + Δr and then average BI3 over Δr so

$$BI3(r,a,z) = \frac{\int_r^{r+\Delta r} BI3(r) 2\pi r \, dr}{2\pi r \, \Delta r} \quad ^*$$

$$= \frac{1}{r\Delta r} \left[(r+\Delta r) BI1(r+\Delta r,a,z) - r BI1(r,a,z) \right] \tag{3.2.5}$$

Thus the current and flux distributions become

$$J_s(r) = - \frac{j\omega\mu_0 \, NI_m a}{2} BI1(r,a,z) \tag{3.2.6}$$

$$B_r(r) = \frac{\mu_0 NI_m a}{2} BI2(r,a,z) \tag{3.2.7}$$

$$B_z(r) = \frac{\mu_0 NI_m a}{2r\Delta r} \left[(r+\Delta r) BI1(r+\Delta r,a,z) - r BI1(r,a,z) \right] \tag{3.2.8}$$

$$B(r) = \sqrt{B_r(r)^2 + B_z(r)^2} \tag{3.2.9}$$

These expressions evaluate the complex amplitudes of the phasors at the

disk surface with I_m the magnitude of the magnetizing current.

---

* $\frac{d}{dx} [X^n J_n(X)] = X^n J_{n-1}(X).$

Evaluating the mutual inductance formula in (2.4.15) using the flux distribution given by (3.2.8) we find

$$M_{12} = \mu_0 N_1 N_2 \sqrt{A_a} \left[(1 + 3C + \ldots) \ln \frac{2}{\sqrt{C}} - (2 + C + \ldots) \right] \qquad (3.2.10)$$

This result appears in reference [8]. It is also very similar to the self-inductance expression (2.4.10) except C is defined differently (see equations 2.4.10 and 3.2.1).

We are now in a position to evaluate the transformer model parameters for which expressions were derived in Chapter 2 (2.4).

(a) Disk Resistance R_D

From (2.4.4), (2.4.5), (2.4.6) and (3.2.6) we have

$$I_{eq} = \int_0^\infty \frac{J_s(r)}{2} \, \delta dr$$

$$= \frac{\omega \mu_0 \sigma N I_m a}{4} \int_0^R BI1(r,a,z) \, \delta dr \qquad (3.2.11)$$

In the numerical integration, the flux density (3.2.9) is evaluated at r and from the magnetization curve $\mu(r)$ is found and δ the skin depth evaluated. R the upper limit of integration is chosen greater than 1.5 times the primary coil radius since outside this radius the current density falls off rapidly and makes little contribution to the integral.

Similarly from (2.4.5)

$$P_D = \frac{\pi}{2\sigma} \int_0^\infty [J_s(r)]^2 \, \delta r \, dr$$

$$= \frac{\pi}{8} (\omega \mu_0 N I_m a)^2 \int_0^R BI1(r,a,z)^2 \, \delta r \, dr \qquad (3.2.12)$$

and so

$$R_D = \frac{P_D}{I_{eq}^2} \qquad (3.2.13)$$

(b) Coil Resistance R_C

As described earlier the d.c. resistance of the coil may be

calculated from the physical dimensions of the coil and conductor

(2.4.7) and a correction applied for a.c.

$$\frac{R_{C\ a.c.}}{R_{C\ d.c.}} = \frac{\Delta}{\delta} \qquad (2.4.9)$$

where Δ is the wall thickness of the hollow conductor.

(c) Coil Self Inductance L_s

We use the formula cited in (2.4.10)

$$L_s = \mu_0 N^2 a \left[(1 + 3C - \frac{15}{4} C^2 + \ldots) \ln \frac{2}{\sqrt{C}} - (2 + C - \frac{31}{8} C^2 + \ldots) \right]$$

$$(3.2.14)$$

$$C = \frac{R}{16a^2} \ ; \ R = 0.2235 \ (b + c')$$

where a is the coil radius, b, c' are the cross-sectional dimensions

of the coil, Figure 1.3(a).

(d) Magnetizing Inductance L_m

$$L_m = [M]_T \ [L_2]^{-1} \ [M] \qquad (3.2.15)$$

We set up inductance matrices for the segments of the disk. The separate

matrices are described in (2.4d).

The mutual inductance M_i between the primary coil and the ith

segment is given by (3.2.10) with $N_1 = N$ the primary coil turns and

$N_2 = 1$.

$$M_i = \mu_0 N \sqrt{ar_i} \left[(1 + 3C - \frac{15}{4} C^2 + \ldots) \ln \frac{2}{\sqrt{C}} - (2 + C - \frac{31}{8} C^2 + \ldots) \right]$$

$$C = \frac{z^2 + (a-r_i)^2}{16ar_i} \qquad\qquad (3.2.17)$$

where r_i is the radius of the ith segment.

The self inductance of the ith segment is given by

$$L_{2\ ii} = \mu_0 r_i \left[(1 + 3C - \frac{15}{4} C^2 + \ldots) \ln \frac{2}{\sqrt{C}} - (2 + C - \frac{31}{8} C^2 + \ldots) \right]$$

$$C = \frac{R}{16r_i^2} \ ; \quad R = 0.2235(\Delta r + \delta)$$

Δr is the width of the ith segment and in keeping with the Poynting

Vector theory of section (2.2) the thickness of the segment is taken

as δ the skin depth.

Finally the mutual inductance between the ith and jth segments

from (3.2.10) is

$$L_{2\ ij} = \mu_0 \sqrt{r_i r_j} \left[(1 + 3C - \frac{15}{4} C^2 + \ldots) \ln \frac{2}{\sqrt{C}} - (2 + C - \frac{31}{8} C^2 + \ldots) \right]$$

$$C = \frac{(r_i - r_j)^2}{16\ r_i r_j}$$

here z the separation is zero.

(e) Leakage Inductance L_ℓ

As before

$$L_\ell = L_s - L_m \qquad\qquad (3.2.20)$$

The computer program used to evaluate the various parameters is described

in Appendix D.

CHAPTER 4

EXPERIMENTAL ANALYSIS

4.1 The Experimental System

In Chapter 3 analytical expressions were obtained for the parameters
of interest in the transformer model, developed in Chapter 2. We now
wish to study a practical system so that a comparison may be made between
experimental and analytical analysis.

The primary coil consists of twenty turns of hollow conductor for
cooling purposes. The physical dimensions are shown in Figure 4.1.
There are two layers of conductor with ten turns per layer. The conductor
is insulated with polyimide film electrical tape which has a high
insulation resistance of class 180°.

The block diagram of the test system is shown in Figure 4.2(b)
and Figure 4.2(a) shows the actual system. The 60 Hz a.c. supply is
rectified and filtered and the d.c. output is fed to a high-frequency
Mapham Inverter[10] which in turn supplies the coil and disk. The inverter
is designed to handle 1500W at 10 kHz, however, provision is made in the
trigger circuit logic to operate at frequencies in the range 7.5-20 kHz
to make frequency studies of the system. The design of the various
components of the system is described in Appendix A. The cooling system
is described in Appendix B. Appendix A also describes the circuit used
to determine the normalized permeability curve used in the computer
calculations.

4.2 Eddy-Current Density and Flux Density Distributions

The analytical expressions for the eddy-current density and flux
density distributions at the disk surface are given by equations (3.2.6),
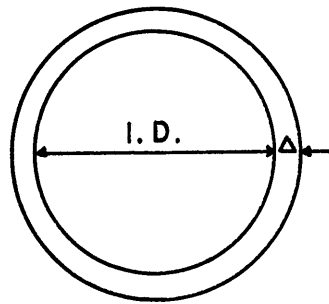
Inner diameter   I.D. = 3.175 mm

Wall thickness Δ = 0.762 mm

Tube mean radius   ac = 2.000 mm

Copper conductivity σ_{cu}=5.9 x 10^7 $(\Omega m)^{-1}$
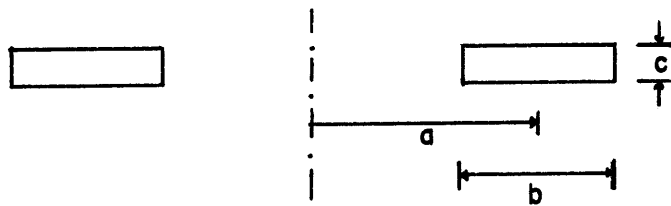
Primary coil radius   a = 9 cm

           width   b = 5.5 cm

          height   c = 1.0 cm

Conductor length   L = 11.3 m

Primary coil turns   N = 20

Figure 4.1   (a) Coil Conductor Dimensions

              (b) Coil Overall Dimensions

Figure 4.2(a)   The Induction Heating System
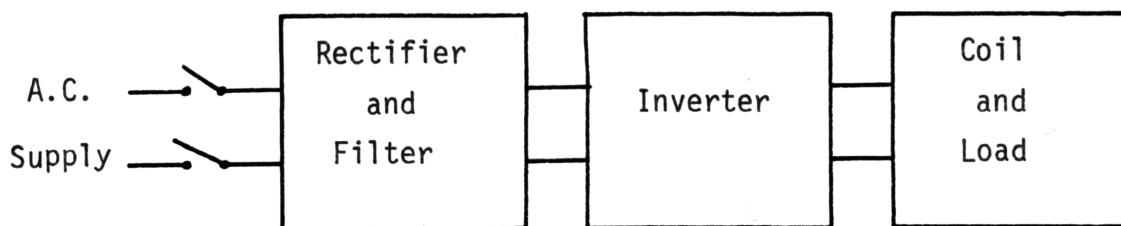
Figure 4.2(b)   Block Diagram of the Induction System

(3.2.7), (3.2.8) and (3.2.9). These equations are evaluated for the experimental conditions at 10 kHz and 2 cm coil-disk separation with the computer program described in Appendix D. The results are plotted in Figure 4.4 for a primary coil magnetizing current of 30A peak or a power of 1000W absorbed in the disk. The flux distribution due to the source alone under the same conditions is experimentally determined to compare the non-interaction approximation developed in chapter 3. Both density distributions are plotted for their respective amplitudes.

It is clear from the current density distribution that our basic assumption of infinite radial dimension in the mathematical model, is valid for disk radii greater than 1.5 times the primary coil mean radius, since the eddy-current density falls off rapidly outside this radius. The power absorbed in the disk is proportional to the integral of the square of the eddy-current density (equation (2.4.5)) and so very little power is absorbed beyond 1.5 times the primary radius.

In Figure 4.4 the total flux density is plotted which is the vector sum of the radial and axial components. Figure 4.3 shows the variation in the axial and radial components. At small radii some error was introduced in the axial component evaluation due to the trapezoidal integration interval used to solve equation (2.2.8) which was chosen for convenience to be one segment wide. Otherwise the distribution is as expected, falling from a maximum at the center of the disk to zero directly over the primary coil, then increasing in magnitude in the negative axial direction to another maximum and finally falling off beyond the coil. The radial component is zero at the center of the coil reaching a maximum over the coil and then falling off beyond the coil
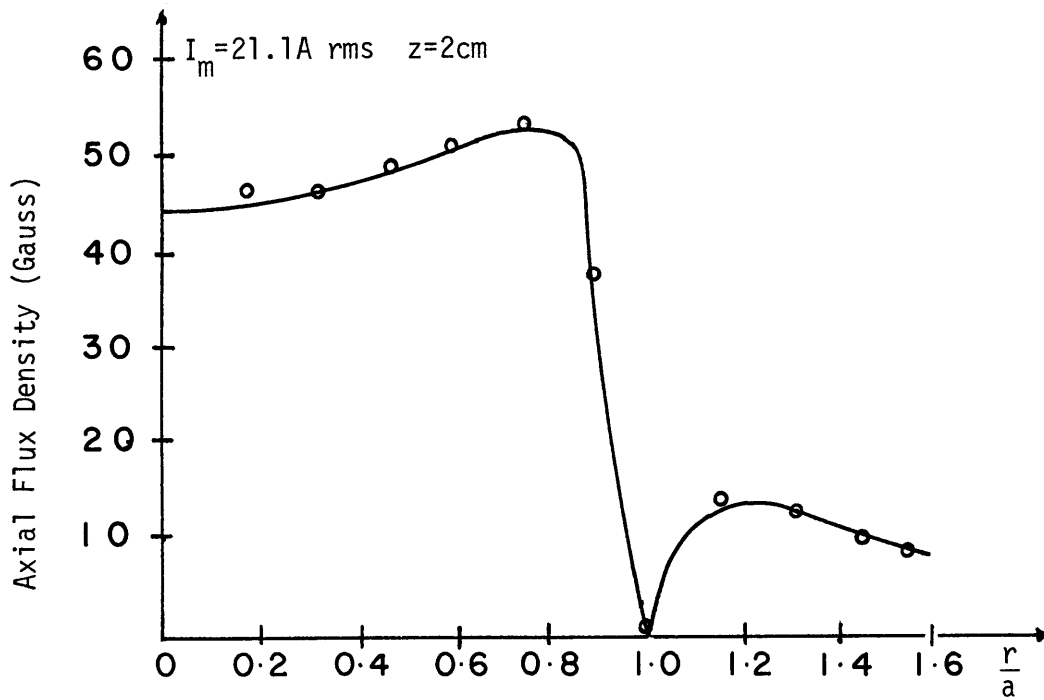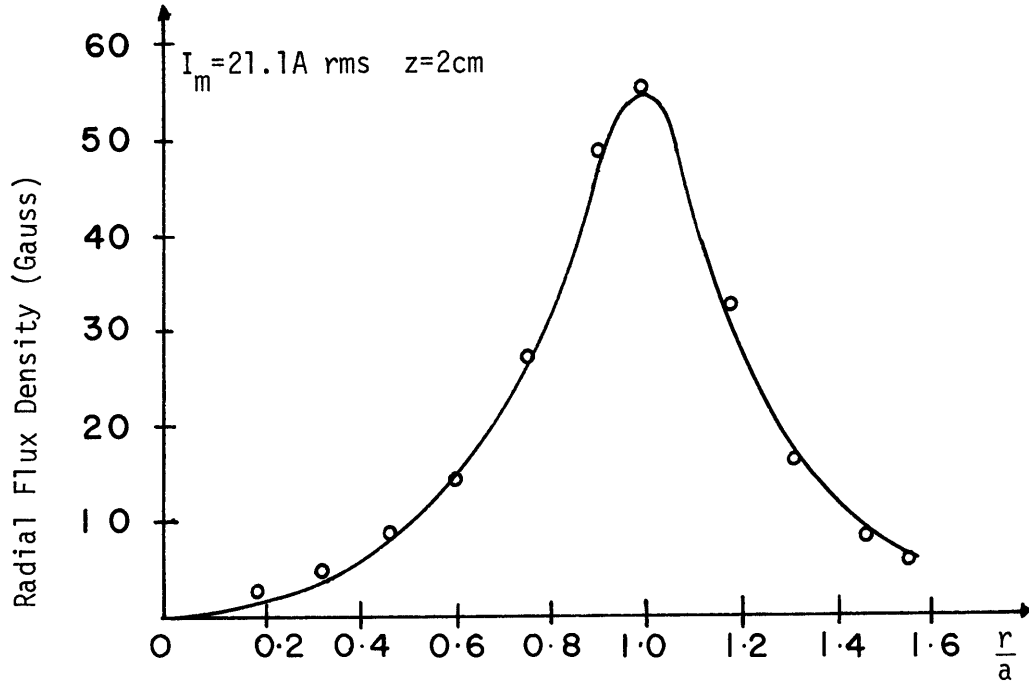
Figure 4.3   Axial and Radial Components of Flux Density
at the Disk Surface

radius. The resultant field has its maximum inside the coil radius. The theoretical curve assumes all the conductors in the primary coil to be concentrated at a mean radius and so we would expect a sharper peak than for the experimental curve of the distributed coil. The actual coil shows a smoother distribution however it is clear that the effect of concentrating the coil is not greatly in error.

The theoretical curve is based on the non-interaction approximation of chapter 3. The experimental curve in Figure 4.4 is measured on no-load, it wasn't possible to measure the flux at the disk surface, however the validity of the approximation is well illustrated by inductance measurements carried out at 1 kHz which showed an increase of 1.6% in the field distribution with the disk placed in the field. The source field was measured at 60 Hz however the source field is independent of frequency. The approximation does depend on frequency since the effect of the eddy-currents increases with frequency.

The amplitude of the total flux density is used to interpolate the relative permeability from the normal magnetization and relative permeability curve of Figure 4.5, the experimental determination of this curve is described in Appendix A3. Table C1 summarizes the data in Figures 4.3 and 4.4.

4.3 Transformer Model Parameters

With the aid of the techniques and expressions described in Chapter 3 the lumped parameters in the transformer model were calculated. Figure 4.6 shows the equivalent model of Figure 2.5 with the calculated values inserted. The value of the equivalent disk resistance is that corresponding to a primary coil current of 30A, it is described in the
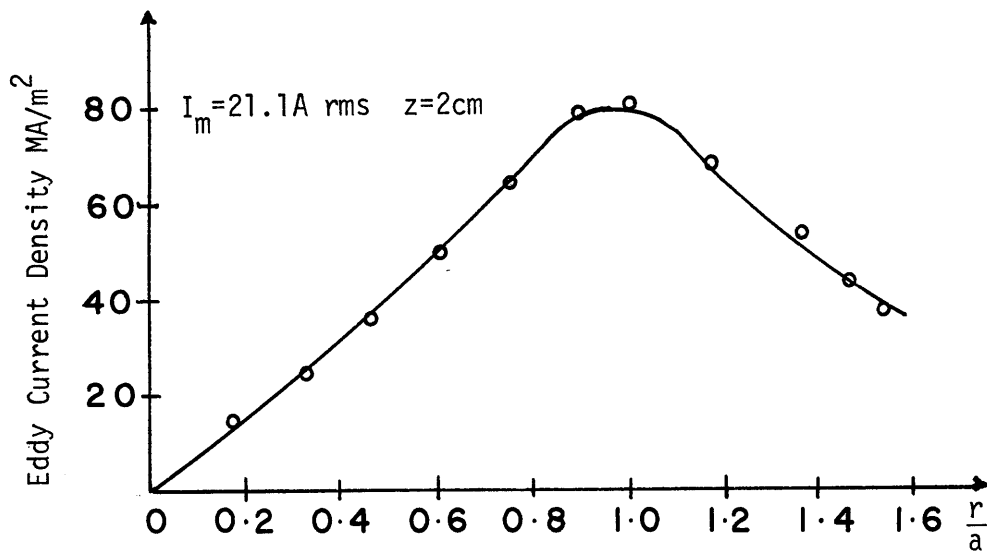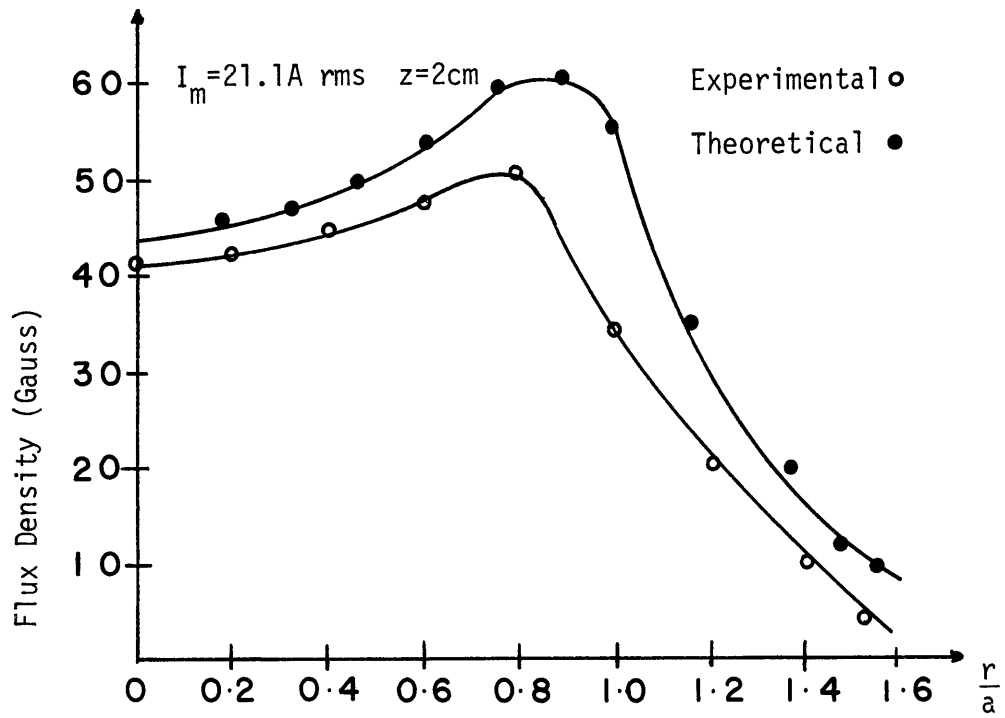
Figure 4.4   Eddy Current Density and Flux Density Distributions
at the Disk Surface
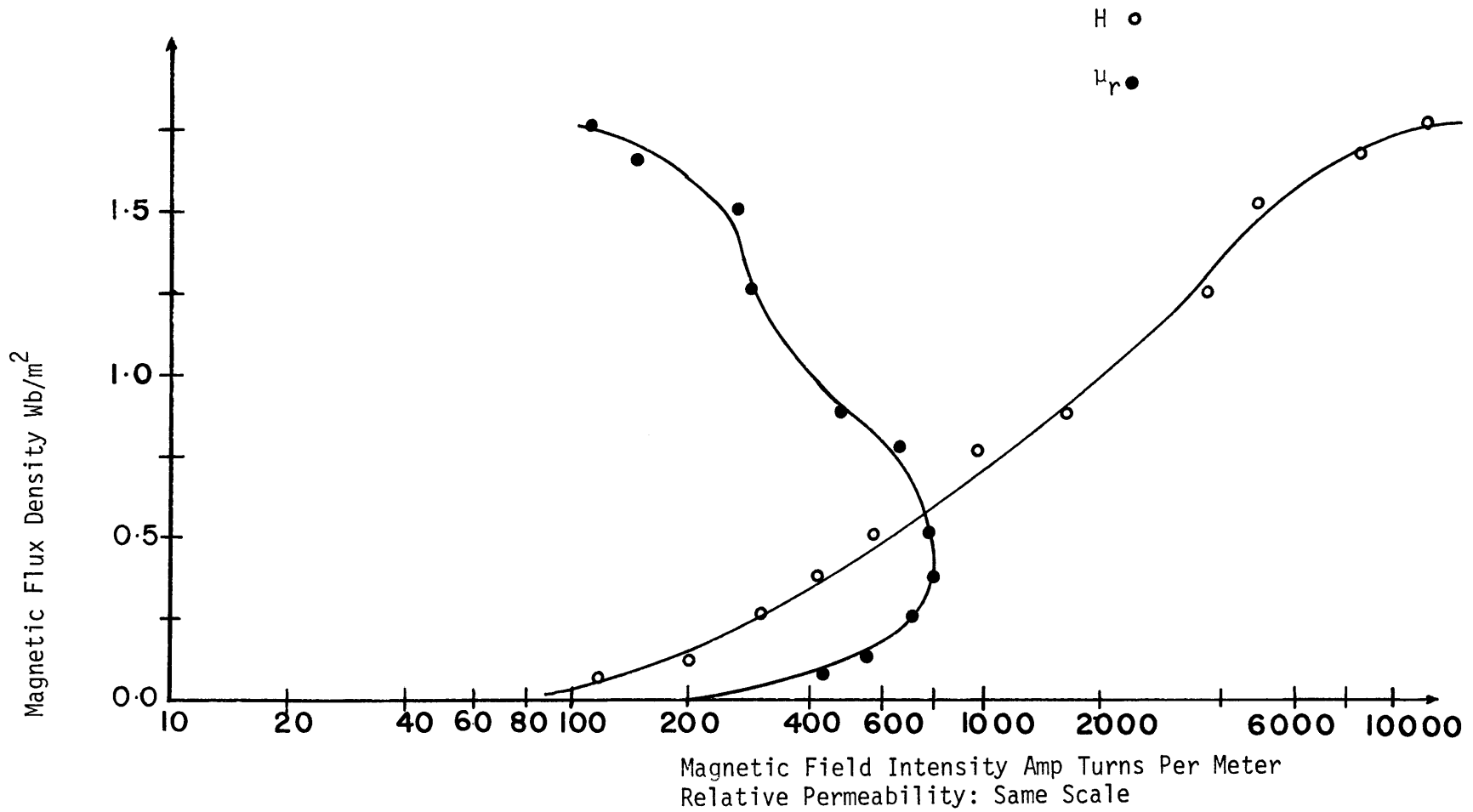
Figure 4.5   Normalized Magnetization and Incremental Permeability Curves for Cold-
            Rolled Steel

next section. The values correspond to a coil-disk separation of 2 cm.

The inductance terms were measured at 1 kHz. An aluminum disk, which

has a high conductivity or low resistance effectively shorts the

magnetizing reactance and so allows the leakage inductance to be

measured. The following results were obtained.

Coil-disk separation: Z = 2 cm

Self-inductance L_s: calculated = 86.9 µH
                     measured   = 92.5 µH

Leakage inductance L_ℓ: calculated = 43.1 µH
                     measured   = 50.5 µH

Magnetizing inductance L_m: calculated = 43.8 µH
                     measured   = 42.0 µH

Coil resistance R_c dc: calculated = 0.020Ω
                     measured   = 0.025Ω

The values are calculated assuming the disk is infinite in the

radial direction. The discrepancy in the leakage inductance is partly

due to the non-ideal short-circuit presented by an aluminum disk. Other-

wise there is very good agreement between measured and calculated values.

The transformer model with the calculated parameters is used in Appendix

A for the inverter design.

4.4 Equivalent Disk Resistance

By specifying the peak magnetization current I_m in equations

(3.2.11) and (3.2.12) then the equivalent resistance R_D of the disk may

be found. With the aid of the phasor diagram of Figure 4.6(c), the

resistance may be plotted as a function of coil current I_p. Table C2

in Appendix C summarizes the data for the test coil, the power dissipated

in the disk is also given for 10 kHz operation. The data is plotted in

Figure 4.7. The non-linear nature of the disk equivalent resistance is

(a)

(b)

(c)

Figure 4.6   (a) Lumped-Parameter Transformer Model
             (b) Equivalent Circuit
             (c) Phasor Diagram
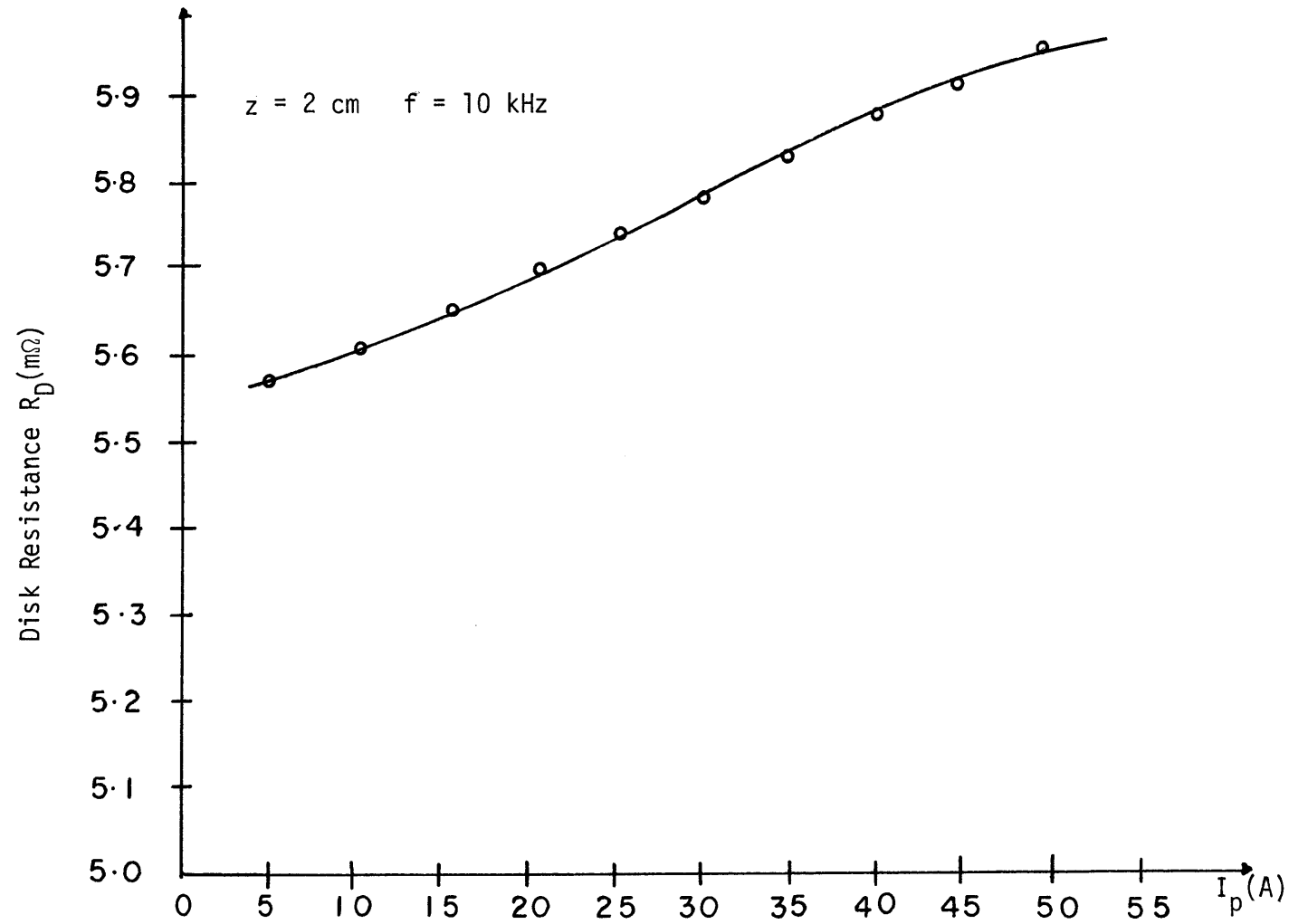
Figure 4.7   Equivalent Disk Resistance as a Function of Primary Coil Current
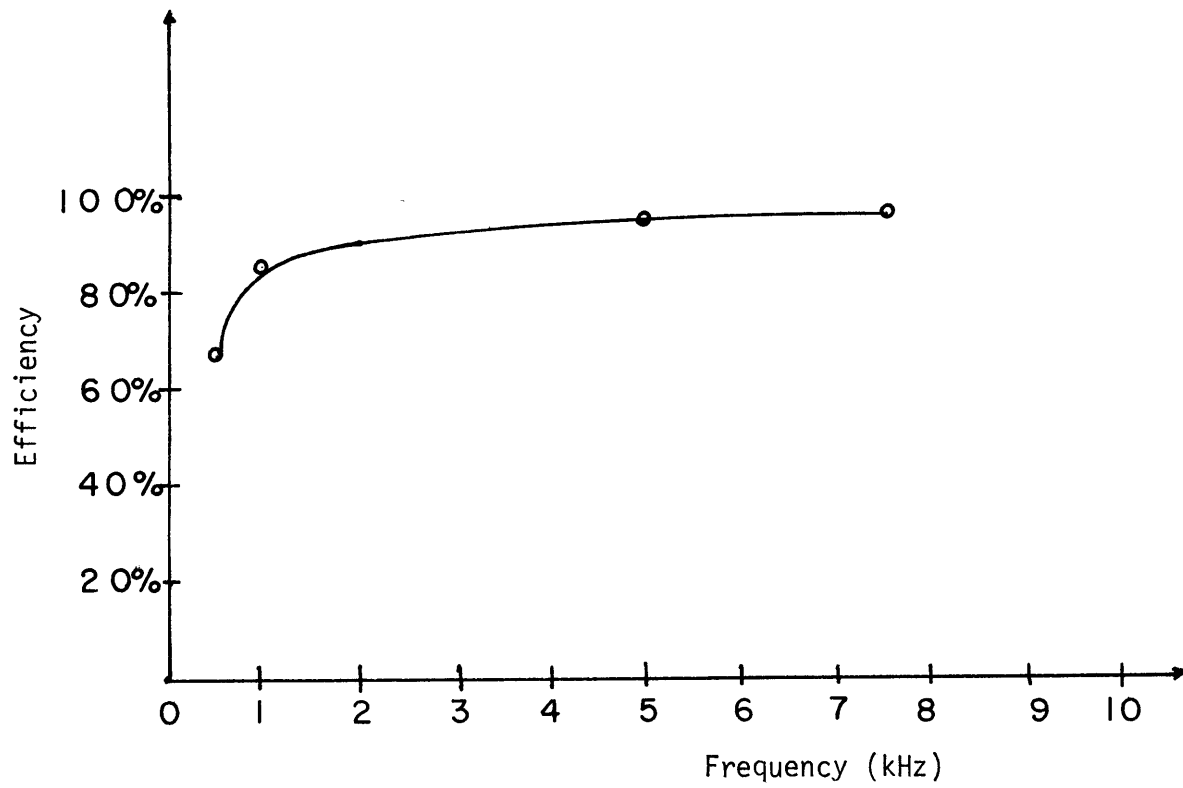
Figure 4.8 Coil-Disk Efficiency as a Function of Frequency

illustrated, reflecting the nature of the permeability curve Figure 4.4.

Equation (2.5.2) is used to plot an efficiency versus frequency curve for the coil disk arrangement. It is shown in equation (2.4.2) that the disk resistance is proportional to the square root of frequency. The inductive reactances are directly proportional to frequency. Figure 4.8 plots the data in Table C3. The plot clearly shows that the efficiency of the system falls off rapidly at low frequencies due to the dissipation in the coil resistance R_C and the shunting effect of the magnetizing reactance X_m. In plotting the curve the d.c. resistance of the primary coil is used at low frequencies when the thickness of the hollow conductor becomes less than the skin depth. The correction for a.c. is applied using equation (2.4.9) which for the coil of Figure 4.1 is

$$R_C \text{ d.c. } = 0.02\Omega$$

$$R_C \text{ a.c. } = 2.32 \times 10^{-4} \sqrt{f} \quad \Omega$$

where f is the frequency in Hz.

4.5 Power Absorbed in the Disk

The power absorbed in the disk is given by equation (3.2.12)

$$P_D = \frac{\pi}{8} (\omega\mu_0 NI_m a)^2 \int_0^k BI1(r,a,z)^2 \, \delta r \, dr \qquad (3.2.12)$$

It is obvious from this equation that the power absorbed in the disk depends on three variables, the magnetizing current I_m, the coil-disk separation z, and the excitation frequency ω or f. The variation with magnetizing current I_m is reflected in the primary coil terminal current I_p which accounts for the effect of the eddy-currents. The test

system was studied for variation in these parameters with each parameter studied separately while the other two are constant. Two disks are studied one having a radius 1.53 timesthe primary coil radius and another with a radius 1.2 times the primary radius. The larger coil satisfies the radial infinite dimension assumption.

Figure 4.9 shows the predicted and experimental power absorbed for both disks, from the data of tables C4 and C5, for a coil-disk separation of 2 cm at 10 kHz. To determine the experimental power absorbed in the disk the voltage, current and phase angle must be measured using a non-inductive sampling resistor having a value R_S = 0.049Ω. To determine the phase angle, the current and voltage are displayed on an oscilloscope (see Figure A.1.2(b) and (c)). 2° is the greatest accuracy at 10 kHz and with the range of phase angles met in the experiments this could lead to errors as great as 10%. To find the actual power absorbed in the disk the following formula is used:

$$P_D = V_p I_p \cos \theta - R_{C \text{ a.c.}} I_p^2$$

From equation (2.4.9) $R_{C \text{ a.c.}}$ = 0.023Ω (calculated) or 0.029Ω (measured).

The agreement between the experimental and theoretical curves is quite good. Much of the error can be ascribed to the method used to determine the phase angle. At high power levels the temperature of the disk rose significantly and the resulting change in resistance was not taken into account in the mathematical model. In the boiling test described in the next section large changes in temperatures were not encountered and better agreement was obtained.

It was shown in section 3.1 that the eddy-current distribution could be found directly from the flux distribution using equation (2.2.8).
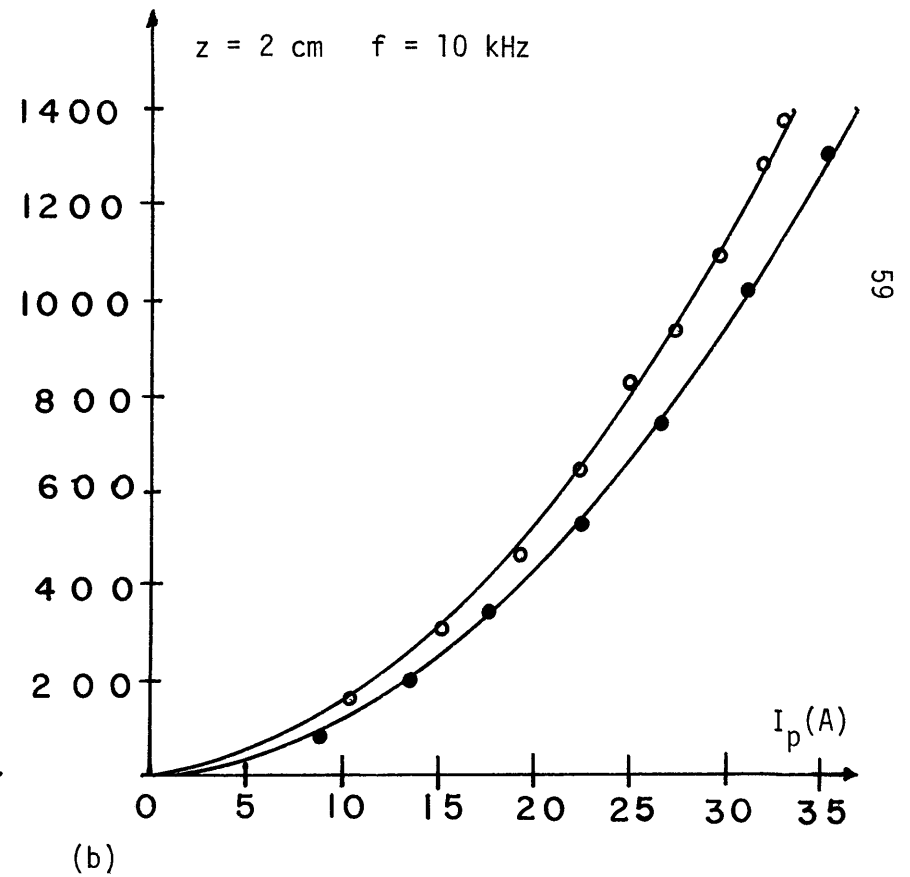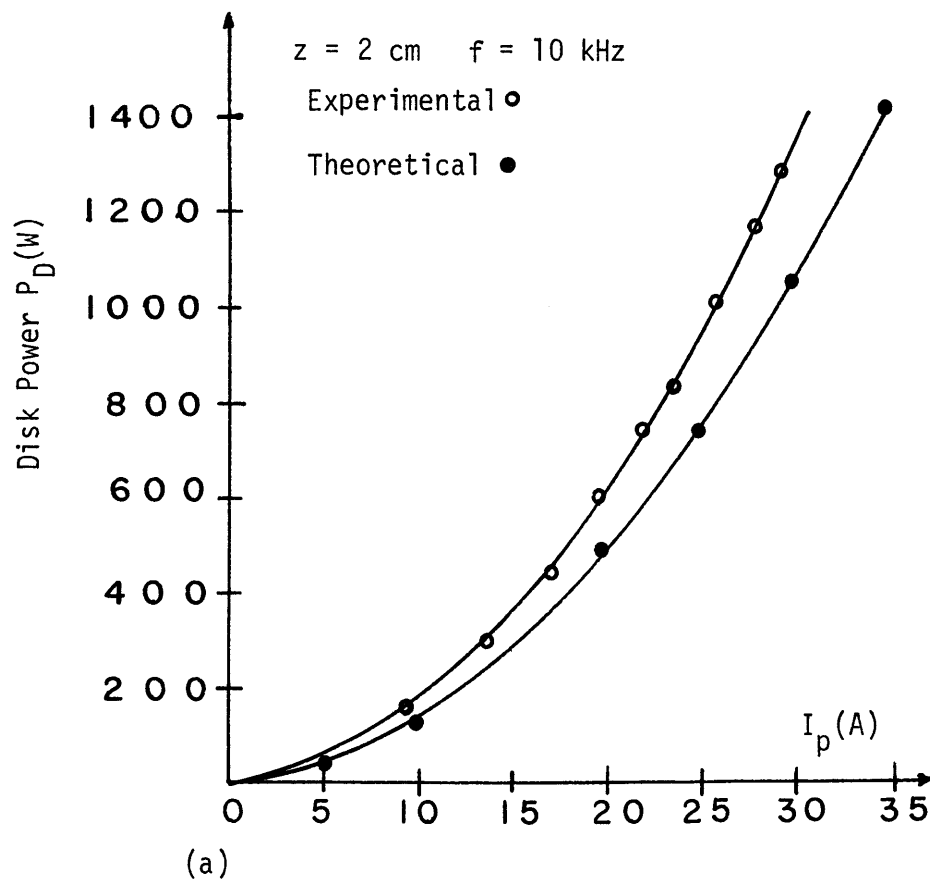
Figure 4.9   Disk Power as a Function of Primary Coil Current
(a) Disk 1: $a_2 = 1.53a$
(b) Disk 2 $a_2 = 1.2a$
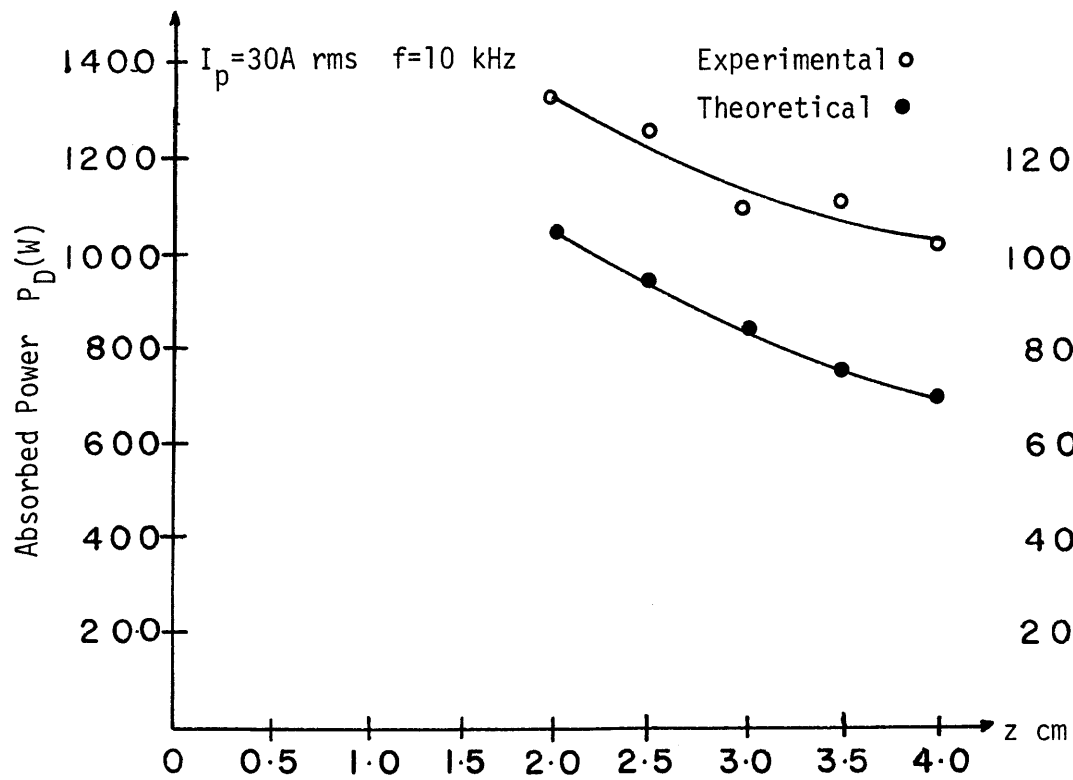
Figure 4.10   Disk Power as a Function of Coil Disk Separation
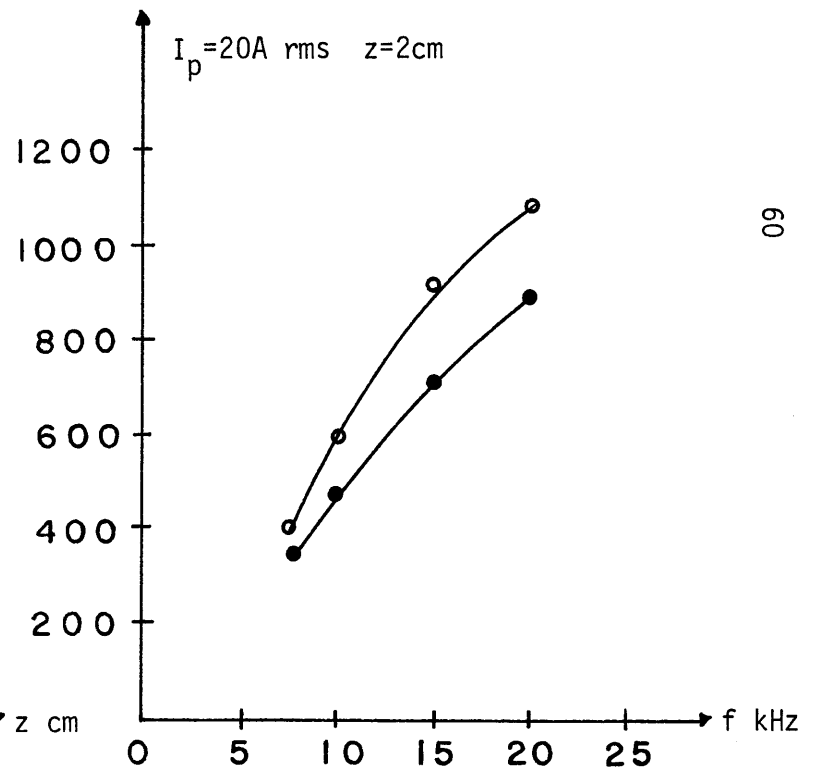
Figure 4.11   Disk Power as a Function of Frequency

This assumes the eddy-currents induced in the disk do not affect the field. Thus if we confine the upper limit of integration to the physical limit of the disk it should be possible to determine the power absorbed. This was done for the smaller disk and the agreement was close. Effectively the non-interaction approximation does not assume infinite radial dimensions whereas the original exact solutions do. The results are plotted in Figure 4.9(b) from the data of Table C5.

The variation in power due to axial separation is shown in Figure 4.10. Both curves show the fall off in power with increased separation. To reduce the current flowing in the primary for a given power level and frequency, the coupling should be as close as possible. In terms of the transformer model this has the effect of reducing the leakage term or increasing the magnetizing term thus reducing its shunting effect on R_D.

The frequency variation in Figure 4.11 again shows that the shunting effect of the magnetizing branch in the transformer model is reduced at higher frequencies so that a larger fraction of the primary current is reflected in the disk. The primary coil resistance also increases with frequency but this is offset by the increased magnetizing reactance. The data for Figures 4.10 and 4.11 is extrapolated from Table C4 for the larger disk for fixed primary current. The extrapolated data is summarized in Tables C6 and C7. Consequently the experimental curves are subject to the same error source as described previously for the separation curves.

As was mentioned in the introduction, water cooling was introduced to improve the coupling between the coil and disk since a fan placed

beneath the coil necessitates a clearance space. The closer coupling allows lower frequencies and currents for the same power. This reduces the switching requirements for the inverter SCR's giving lower component costs.

The overall efficiency of the system can be determined from the data of Table C4. In making the calculation the power absorbed in the sampling resistor must be subtracted so

$$P_{a.c.} = P_{in} - R_s I_p^2$$

$$\eta_0 = P_D/P_{a.c.}$$

$$= \frac{V_p I_p \cos\theta - R_{C\,a.c.} I_p^2}{P_{in} - R_s I_p^2}$$

For 1500W input the overall efficiency between a.c. input and absorbed disk power is 75%. The efficiency does not increase with frequency despite increased η_{CD}. The reduced efficiency is mainly due to increased switching losses at higher frequencies.

4.6 Time of Boil Test

The practical application of induction heating to the induction range was described in the introduction. The boiling test is conducted to demonstrate the advantages of the range over conventional devices. A comparison is made between the induction range and a conventional resistance heating element hot-plate. Both units are tested under the same experimental conditions.

Two liters of water are boiled on the induction range using a vessel whose base has the same material as used in previous experiments i.e. cold-rolled steel. The a.c. power input was 1500W with 1100W at the primary coil terminals. The test was carried out at 10 kHz with

a coil-disk separation of 2 cm. Figure 4.12 shows the temperature rise of the water as a function of time. We define the effective heating rate P_E as

$$P_E = mC_p \frac{dT}{dt}$$

where m is the mass of the water and C_p is its specific heat.[*] The temperature derivative is taken in the linear region of the boiling characteristic. We define the load efficiency as

$$\eta_L = \frac{P_E}{P_{CD}}$$

where P_{CD} is the electric power at the coil terminals. Finally we define our overall efficiency as

$$\eta_o = \frac{P_E}{P_{a.c.}}$$

where $P_{a.c.}$ is the a.c. power input from the supply.

The test was now repeated for the electric ring at both 1500W and 1100W input. It is difficult to specify exactly when boiling occurred but for comparison purposes we will define it here as the time taken to reach 90% of the final temperature.

Table 4.1 summarizes the results for the three tests.

The load and overall efficiencies are equal for the electric ring since we assume all the a.c. power goes directly to the terminals of the ring. In the induction range the difference between η_L and η_o reflects the power loss in the inverter and rectifier circuit. From the terminal view η_L shows the induction range is far more efficient in transferring

---

[*]Water at 60°C: density ρ = 985.4 Kg/m³, C_p = 4184 J/kg °C.
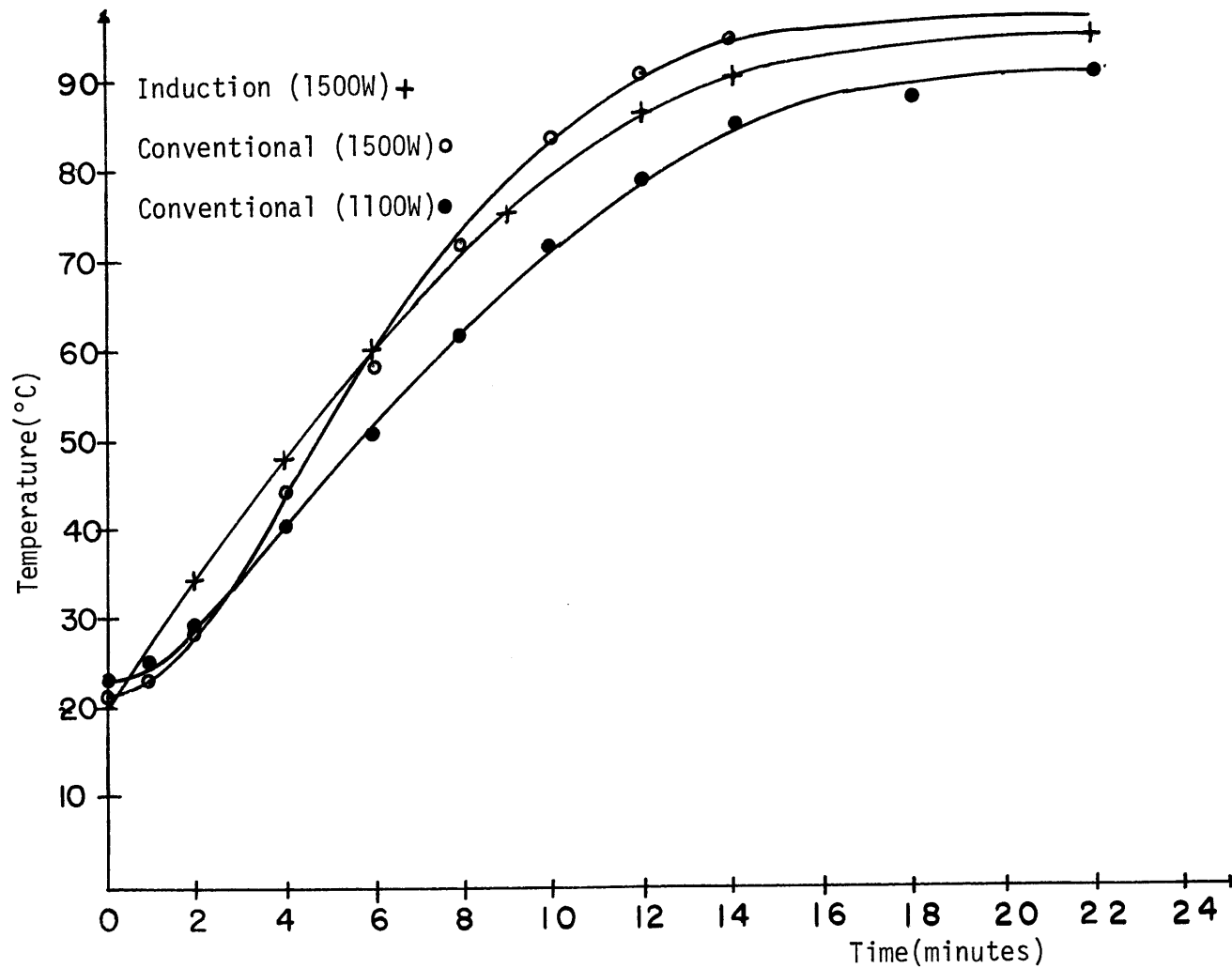
Figure 4.12   Temperature Rise Characteristics of Induction and Conventional Ranges

Table 4.1

Time to Boil Test for the Induction and Conventional Ranges

Type	$P_{a.c.}$ (W)	P_E (W)	η_L	η_o	Time to Boil (min)
Induction	1500	893	81.2%	59.5	12.6
Electric ring	1500	962	64.1%	64.1	11.2
Electric ring	1100	722	65.6%	65.6	14.2

energy from the primary element to the heated element. In terms of a.c. input the induction range is slightly less efficient but this situation can be improved by better inverter design. In terms of time to boil the induction range is faster for the same power at the primary element terminals and marginally slower with the same a.c. supply input due to the circuit losses not present in the conventional stove.

Figure 4.12 illustrates the effect of thermal inertia on the response of the respective stoves. For the induction range the load temperaure increases immediately when the power is switched on whereas the ring has a delay due to thermal capacity and cannot transfer heat to the load until it has first heated itself. After the initial delay the effective heating rated is higher for the same a.c. input. The curve for the induction appliance seems to be much slower that the electric range near boiling. This is due to heat being convected from the hot disk back to the cool coil, not present in the conventional range. This tends to offset the advantage gained at starting. Improved design would eliminate this effect by thermally insulating the cooking vessel from the exciting coil. It is interesting to note that when the load was removed from the induction range the coil was near room temperature whereas the

electric ring was in excess of 100°C, reflecting the effect of a thermal

contact resistance not present in the induction range. More elaborate

and extensive comparisons are made in references (1) and (3).

CHAPTER 5

CONCLUSIONS AND RECOMMENDATIONS

The coil-disk arrangement studied here is a relatively simple
geometry where the solutions to the field equations could be reduced to
one dimension or in some cases two. However, the development of the
lumped-parameter transformer model is a powerful tool whereby more
complicated geometries could be handled, adopting the same techniques
developed here. In general, the correlation between experimental and
analytical analysis was quite good over a very wide range of experiments.
The non-interaction approximation described in Chapter 3 proved to be
a very useful method in simplifying the complex field and current density
equations without greatly affecting the integrity of the analysis.

The model could be refined to eliminate a number of error sources.
The variation of the disk equivalent resistance with temperature should be
included as should the distributed nature of the exciting coil by adopting
the segment technique used for the disk. This would be useful for the
design of coils with uniform fields. Hysteresis loss which has a greater
effect at high frequencies should also be included. All these refine-
ments would tend to increase the absorbed disk power reducing the error
in Figure 4.9. The experimental errors were largely attributed to the
phase angle measurement at the coil terminals. It should be possible to
build a high frequency phase detector using phase-lock loop techniques
and digital counters.

In the analysis presented here, one material was studied. The
computer program developed in Appendix D could be used to study any
material for which a B-H curve is available and its conductivity.

The application to the induction range was mentioned in the
Introduction. Much development is needed. The introduction of an
insulator between the coil and disk would eliminate "back heat" (section
4.6) and perhaps forced convection cooling would not be required.
Temperature sensing elements would be needed to give control of operating
temperatures. This could be achieved by coupling to the logic circuit
to vary frequency or using phase controlled rectifiers with the firing
angle determined by temperature.

APPENDIX A

CIRCUIT DESIGN

A1 High Frequency Inverter

The circuit diagram of the SCR sine-wave inverter used in the test system is shown in Figure A1.1. A detailed description of the operation and design of the circuit is given in reference [10]. The 60 Hz a.c. supply is rectified using a center-tapped transformer and a bi-phase half-wave rectifier. The rectifier output is filtered to eliminate inter-modulation distortion at the output of the inverter feeding the coil and disk. The filter output is shown in Figure A1.2(a) for one half of the center tapped capacitor with a load corresponding to 1100W disk power or 1500 at the a.c. input. The waveform indicates less than 5% ripple. The circuit is designed to handle 1500W at 10 kHz with provision made for frequency variation.

Each half of the center-tapped capacitor is charged to a d.c. voltage E. When SCR_1 is triggered current flows from the top capacitor to the load capacitor C charging it to a voltage approaching 2E. The current then reverses flow back to the supply voltage E via diode D_1 and the load capacitor discharges. The reverse current flow presents turn-off to the SCR. Now SCR_2 is triggered and a similar cycle occurs for the lower half of the center-tapped capacitor. SCR_1 is again triggered and the complete cycle repeats. Figure A1.2(d) shows the current through SCR_1 and D_1. The output voltage and current waveforms and trigger pulses are also shown. The waveforms apply for 10 kHz operation with an a.c. input of 1500W and z = 2cm. There is some distortion present in the output current waveform due to the switching
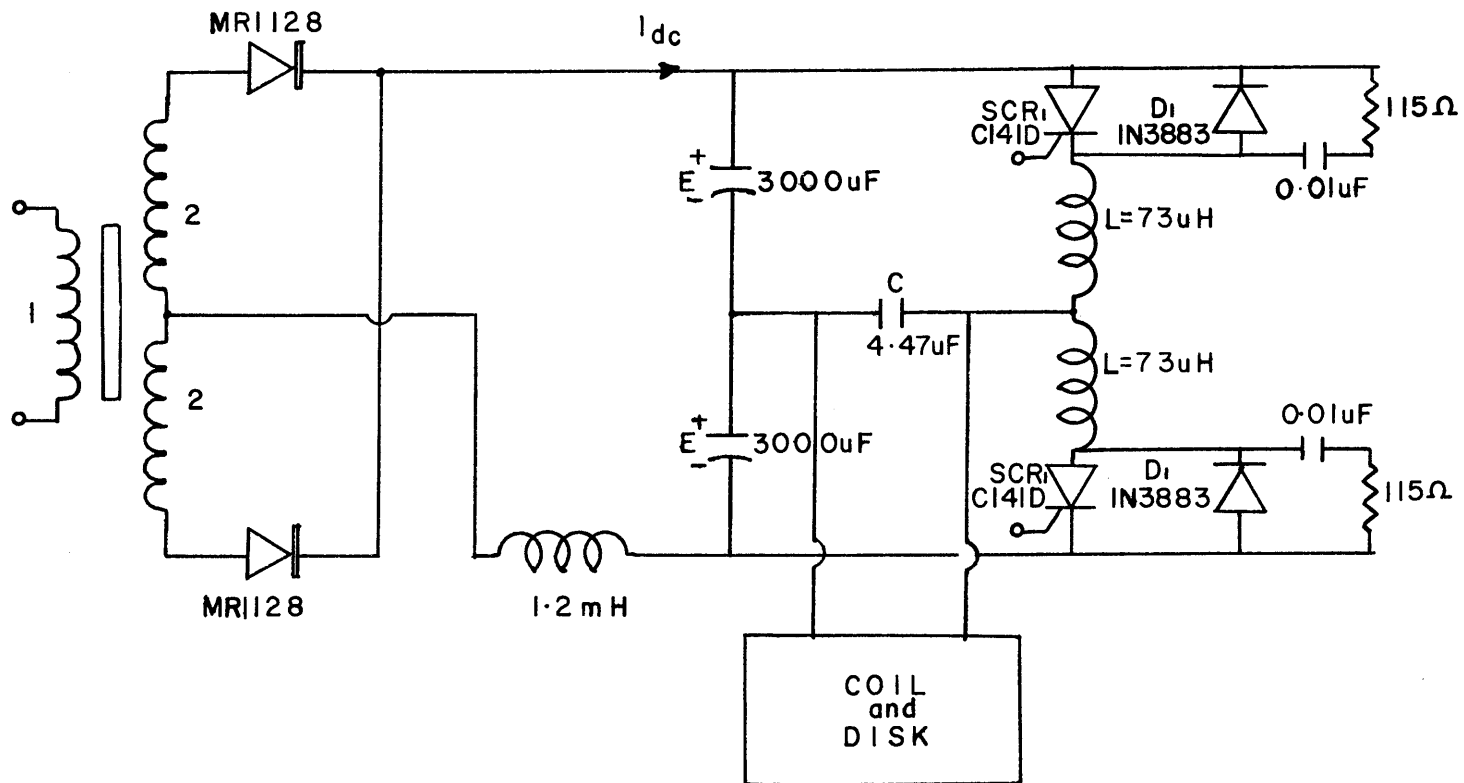
Figure A1.1   SCR Sine-Wave Inverter

71
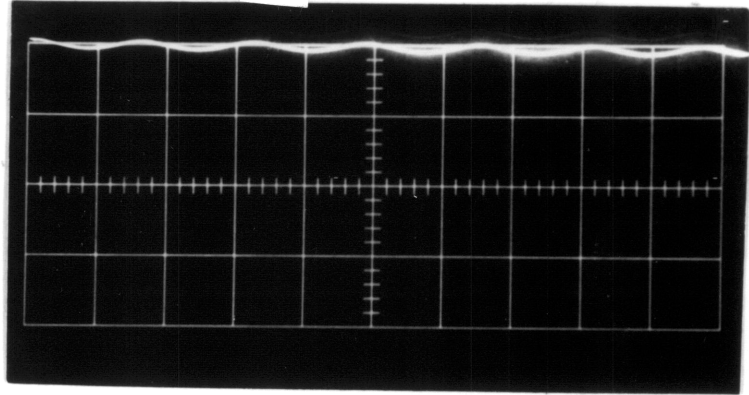
Figure A1.2(a)   Filter Output Voltage
                Scales: Horizontal: 5μs/div.
                        Vertical: 50V/div.
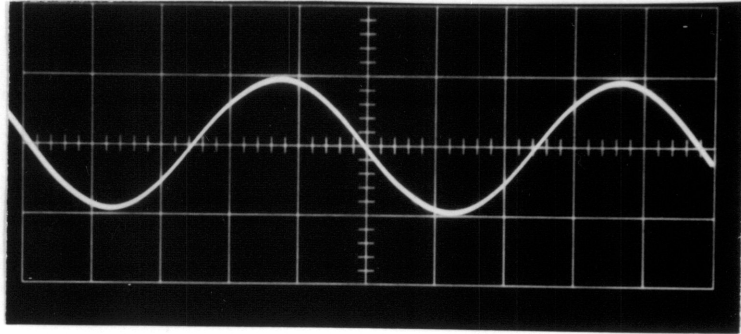
Figure A1.2(b)   Inverter Output Voltage
                Scales: Horizontal: 20μs/div.
                        Vertical: 400V/div.
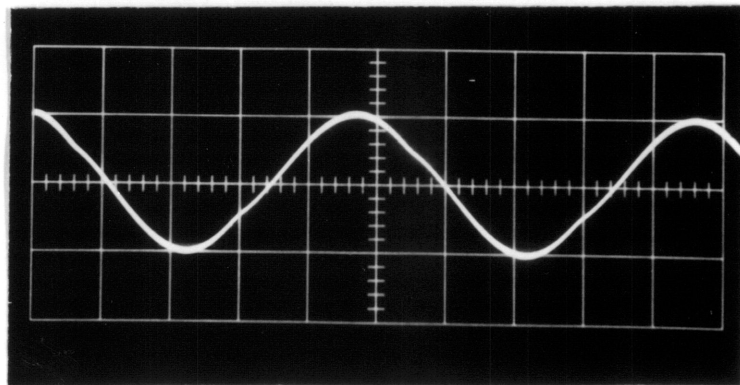
Fig. A1.2(c)   Inverter Output Current
              Scales: Horizontal: 20μs/div.
                      Vertical: 40A/div.
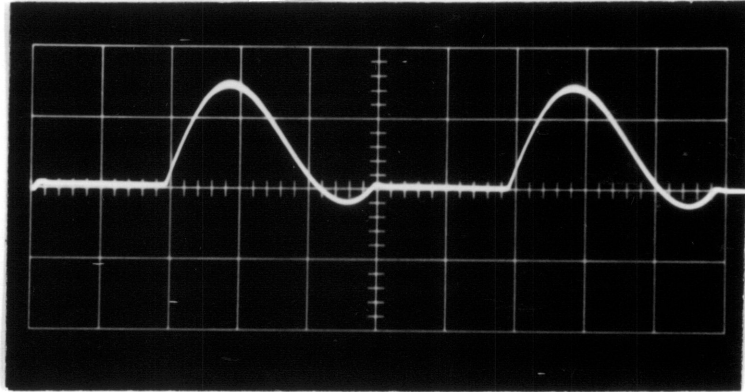
Figure A1.2(d)   SCR and Diode Current

        Scales: Horizontal: 20μs/div.
                Vertical: 20A/div.
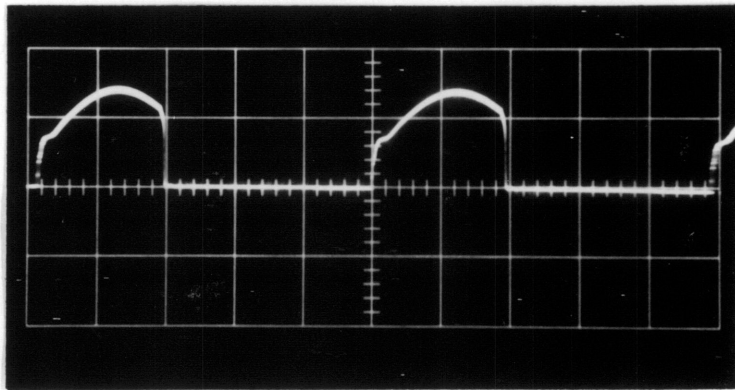
Figure A1.2(e)   SCR Anode-Cathode Voltage

        Scales: Horizontal: 20μs/div.
                Vertical: 200V/div.
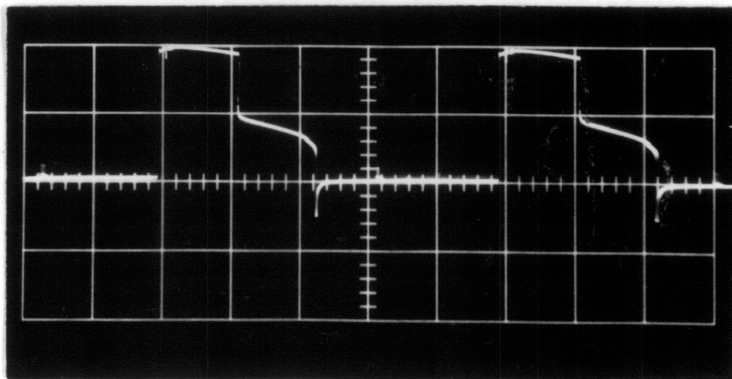
Figure A1.2(f)   SCR Gate Voltage

        Scales: Horizontal: 20μs/div.
                Vertical: 1V/div.

of the SCR's in the resonant LC circuit. Figure A1.2(d) shows the damping effect of the load resistance.

To optimize the design of the inverter as described by Mapham[10] the transformer model is extremely useful. Figure A1.3 shows the equivalent transformer circuit and an equivalent parallel circuit. The reflected disk resistance R_R corresponds to 1000W absorbed in the disk and is taken as a representative value. The equivalent parallel inductance of Figure A1.3(b) is combined with the inverter inductance and capacitance C to give a resonant frequency approximately 1.35 times the output frequency which is the optimum value for minimum output waveform distortion. The load inductance chosen for the design corresponds to z = 2cm. The transformer model predicts the terminal voltage and current, using these values in conjunction with the design tables calculated by Mapham the device ratings are found.

For the values indicated in Figure A1.3 the following information is extracted from the design tables and compared with the results in Figure A1.2, which apply to the design conditions. All values are rms unless otherwise stated.

Input power P_{in} = 1500W

Output frequency f_o = 10 kHz

Coil-disk separation z = 2 cm

Resonant inductance L = 35.5 μH (73||69)

Resonant capacitance C = 4.47 F

Resonant frequency f_r = 12.6 kHz

D.C. supply voltage E = 100V

D.C. supply current I_{dc} = 7.5A $(\frac{P_{in}}{2E})$
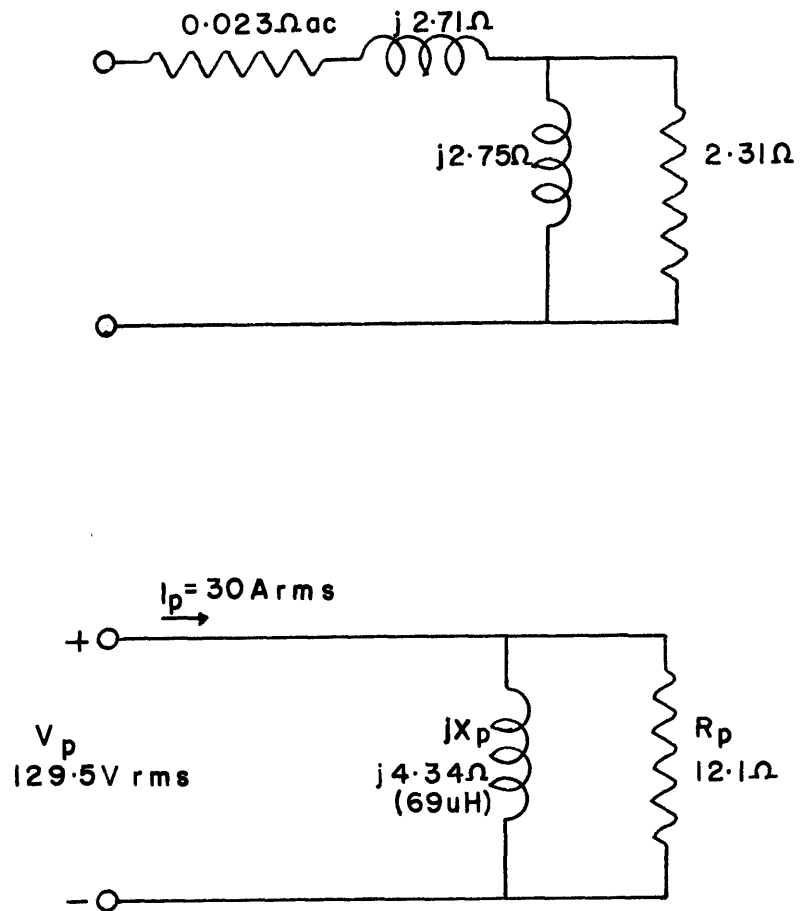
Figure A1.3   (a) Transformer Model

(b) Equivalent Parallel Circuit

Load resistance R = 12.1Ω

f_r/δ_0 = 1.26; R/$\sqrt{4c}$ = 4.3.

Maximum load voltage = 200V
    (Fig. A1.2(b) - 200V)

Maximum SCR voltage = 360V
    (Fig. A1.2(e) - 280V)

Peak SCR current = 50A
    (Fig. A1.2(d) - 28A)

Worst case SCR turn-off time = 15.8 μs
    (Fig. A1.2(d) = 16 μs)

Thus the circuit was driven almost to its limits at 1500W. The

d.c. filter output 2E = 200V gives 70.7V rms at the transformer primary

for a 1:2 turns ratio. The transformer turns (86 in primary) are

chosen to give a maximum flux density in the core of 1.3 Wb/m^2 with

120V rms impressed on the primary. The transformer is wound on a 12 mil

selectron C core AA 526, the inductors are wound on Arnold cores A126040-2

with 41 turns each. The snubber circuits[11] are included to prevent SCR

turn on due to the large dV/dt introduced by oscillations when the free-

wheeling diode turns off.

The circuit is basically a parallel resonant circuit with the load

capacitance C in parallel with the resonant inductance and the equivalent

parallel resistance R_p of Figure A1.3. The SCR current must be under-

damped with a resonant frequency greater than the output frequency so

that when the oscillating current reverses diode D_1 conducts to turn-off

SCR_1 before SCR_2 is triggered. To improve the oscillation the Q-factor

(ωRC) should be as large as possible. Since the resistance is fixed by

the disk, improvement can be accomplished by increasing C. C was chosen

to ensure underdamped oscillations while at the same time maintaining

turn-off time for the SCR and keeping the maximum SCR voltage within the rated limit.

A2 Trigger Logic Circuit

The trigger circuit and associated timing waveforms are shown in Figures A2.1 and A2.2. An astable multivibrator with an external variable resistance and capacitance is used to generate a clock pulse. The resistance is varied so that the clock frequency is double the desired output frequency in the SCR's. A T flip-flop is used with both inputs of a J-K flip-flop connected high. The output changes state with the arrival of the positive-going edge of each clock pulse. The clock is then ANDed with the outputs Q and $\bar{Q}$ of the flip-flop. The timing diagram shows the outputs of the AND gates with two pulse trains each having a frequency of half the clock frequency. This scheme was chosen to ensure that the two pulse trains which supply the SCR gates would not have two pulses occurring simultaneously, switching both SCR's and short-ing the power supply. The clock is delayed through two inverters and a 0.01 µF capacitor to off-set the propagation delay in the flip-flop.

The two pulse trains of Figure A2.2 are buffered and inverted for compatability between CMOS logic in the train generation and the TTL used for amplification. A hex inverter with open collector connects the train to the input of an optical isolator. The output of the isolator is connected to the supply through a 270Ω resistor to give a photo-darlington connection. The base of the first transistor is connected through a 2.7k resistor to ground which helps remove space charge from the base of the second transistor to speed up turn-off. The output of the optical isolator drives an emitter follower and the resultant output is connected
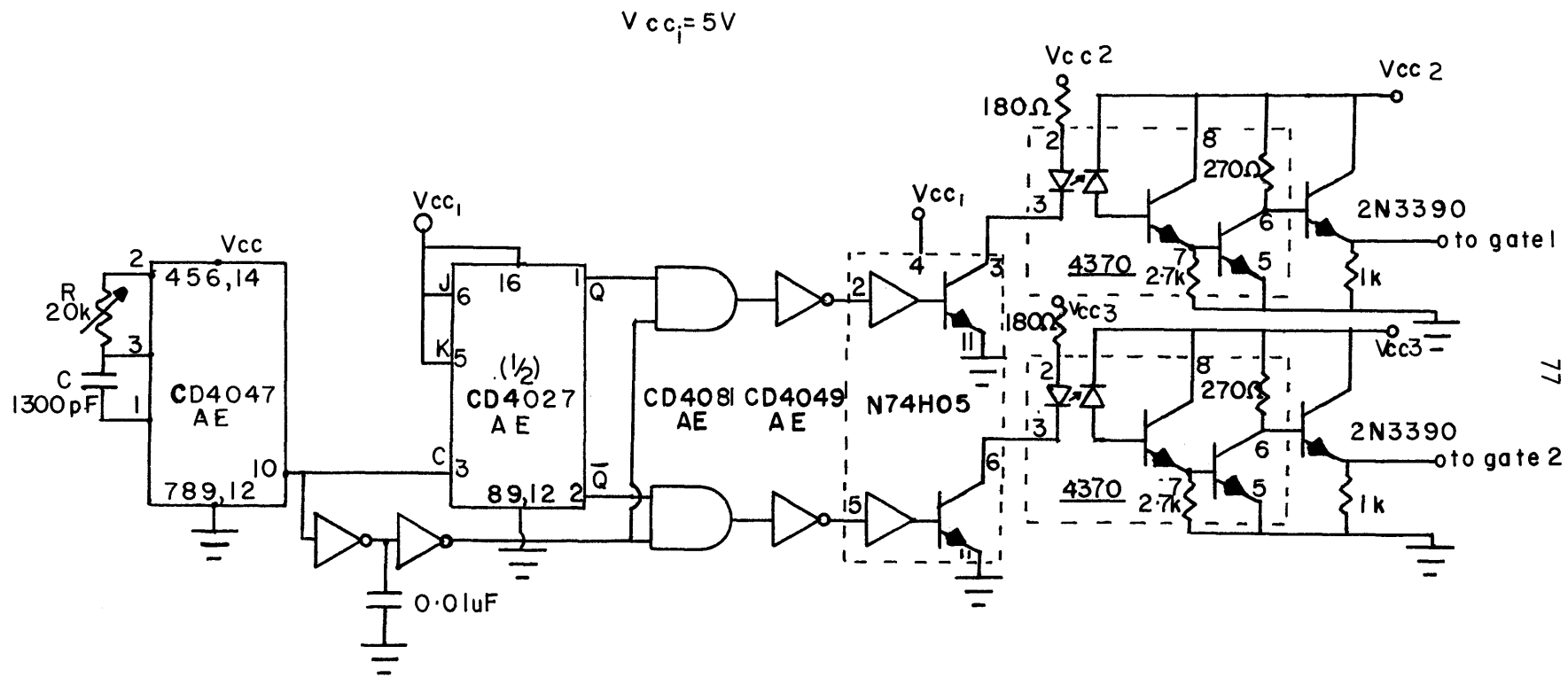
Figure A2.1 Trigger Logic Circuit
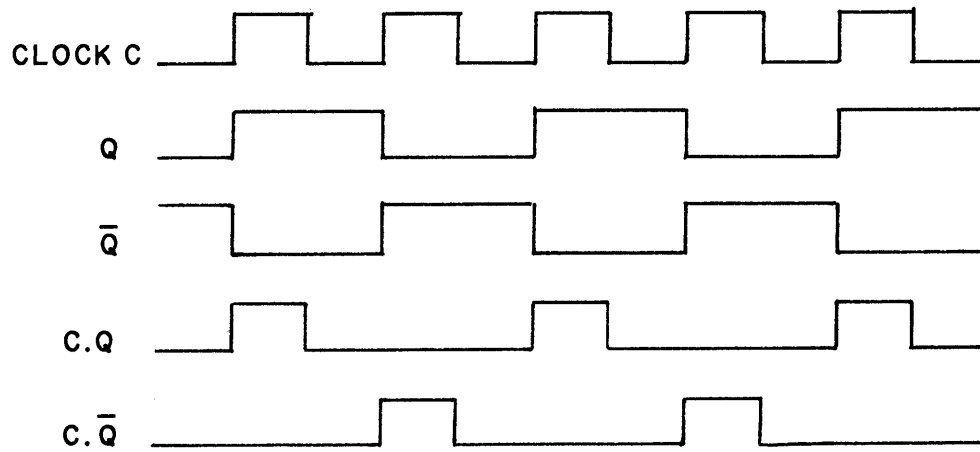
Figure A2.2 Trigger Circuit Timing Waveforms

to the gate of the SCR. The 1k resistor in the emitter follower de-
sensitizes the gate to stray charges and shunts dv/dt currents which
may turn on the SCR. The output of the emitter follower is simply an
amplified version of the AND gate output shown in Figure A2.2. The
current gain of the optical isolator is typically 700 while the emitter
follower transistor is also high gain ($h_{FE} \sim 400$). This reduces the
drive requirement at the input of the isolator. For convenience a five
volt supply was used for all parts of the circuit.

A3 Experimental Determination of the Normal Magnetization Curve for a Ferromagnetic Material

In order to determine the magnetization curve and the incremental
permeability, the hysteresis loop of the material is displayed on an
oscilloscope.

Consider the test specimen shown in Figure A3.1 with a terminal
voltage v and current i. The test piece consists of toroidal
laminations with a winding of N turns.

Equation (1.1.1) in integral form becomes

$$\oint_C \bar{H} \cdot d\bar{\ell} = \int_S \bar{J}_f \cdot \bar{n} \, da \qquad (A3.1)$$

So the magnetic field intensity in the core is

$$H = \frac{Ni}{\ell_m} \qquad (A3.2)$$

where ℓ_m is the mean length of the magnetic path in the specimen.

The flux linking the coil is

$$\lambda = N \int \bar{B} \cdot \bar{n} \, da$$
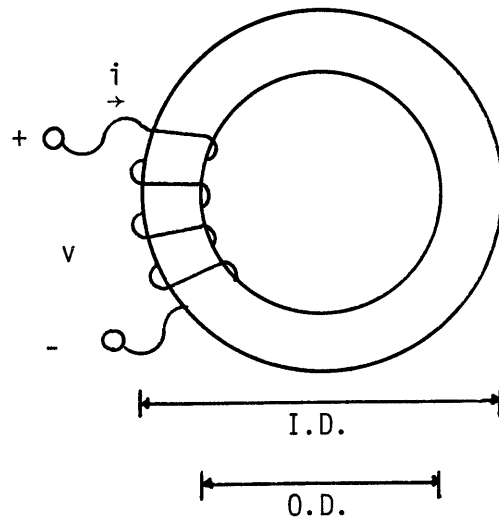
Inner Diameter	I.D. =	4.51 cm
Outer Diameter	O.D. =	6.25 cm
Lamination Thickness	d =	0.265 cm
Core Thickness	t =	0.8 cm
Number of Turns	N =	500
Winding Resistance	R_W =	1.4Ω
Core Conductivity	σ =	6.7×10^6 $(\Omega m)^{-1}$
Typical permeability	μ_r =	600
Skin Depth at 60 Hz	δ =	0.10 cm

Figure A3.1   Test Specimen Data for Normalized
                      Magnetization Curve.

$$= NB \ A_C \qquad (A3.3)$$

where B is the magnetic flux density in the core of cross sectional area A_C.

From Faraday's Law, assuming negligible winding resistance

$$v = \frac{d\lambda}{dt} \qquad (A3.4)$$

we obtain the flux density

$$B = \frac{1}{NA_C} \int v dt \qquad (A3.5)$$

Thus it is necessary to integrate the voltage at the terminals of the coil.

The ideal closed loop gain of the inverting integrator shown in Figure A3.2(a) is[12]

$$\frac{V_o}{V_i} = - \frac{1}{R_1 CS + \frac{R_1}{R_2}} \qquad (A3.6)$$

If $R_2 \gg R_1$

$$\frac{V_o}{V_i} = - \frac{1}{R_1 CS} \qquad (A3.7)$$

R_2 is present to prevent voltage build-up on the capacitor, it is chosen large enough so that integrator behavior is unaffected.

The practical circuit is shown in Figure A3.2(b). There is a 100:1 attenuator at the input so that large signals may be handled by the integrator operational amplifier. A buffer is included to increase the input impedance of the integrator so that ideal conditions are approached. Offset and balance circuits are also included. The resistor and capacitor
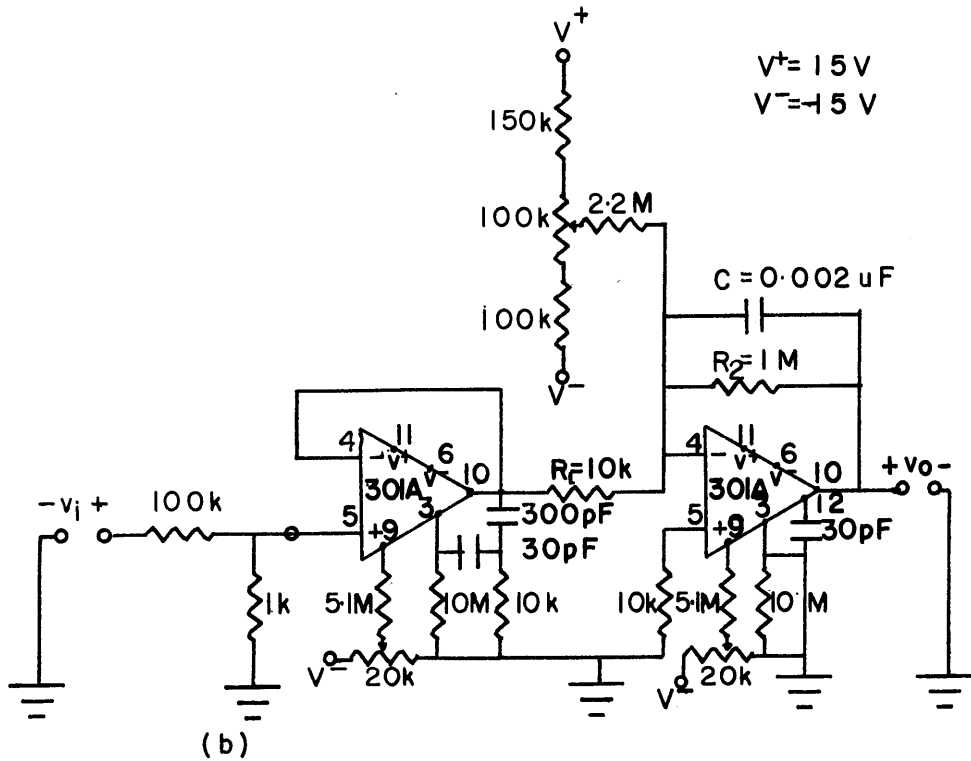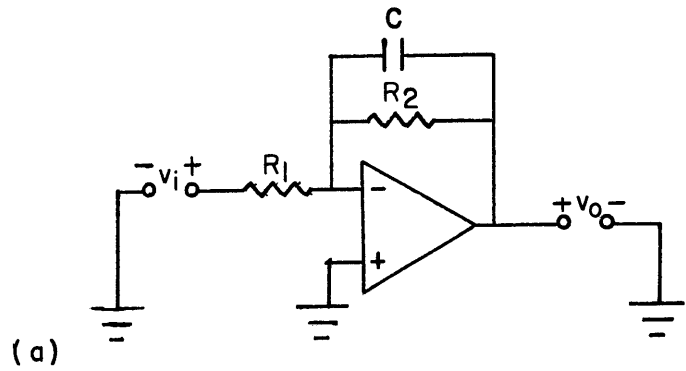
Figure A3.2 Inverting Integrator

values for the integrator are chosen so that the singularities of the loop transmission are well removed from the test frequency 60 Hz. (With the values shown, the singularities occur at 7.2 Hz and 720 Hz).

With the dimensions shown for the test piece and the circuit values in the integrator (A3.2) becomes

$$H = 2.958 \times 10^3 i \text{ At/m}$$

where i is measured in amperes.

From (A3.5) and (A3.7) we have

$$B = 0.63 \ v_0 \ \text{Wb/m}^2$$

where v_0 is the output voltage of the integrator in volts.

The current and voltage can be displayed on an oscilloscope. Figure A3.3 shows a hysteresis loop for cold rolled steel with appropriate scale factor applied. The incremental permeability is got by dividing the maximum values of B and H at the tip of the hysteresis loop. Table C9 summarizes the results for cold rolled steel and the results are plotted in Figure 4.5. The relative incremental permeability is also plotted.

The conductivity of the disk material is found from d.c. voltage and current measurements made on a bar of the material of known length (ℓ) and cross-section (A_b).

$$\sigma = \frac{1}{R} \ \frac{\ell}{A_b}$$

where R is the resistance.

For cold-rolled steel it was found to be, from the data in Table C10

$$\sigma = 6.7 \times 10^6 \ (\Omega m)^{-1}$$
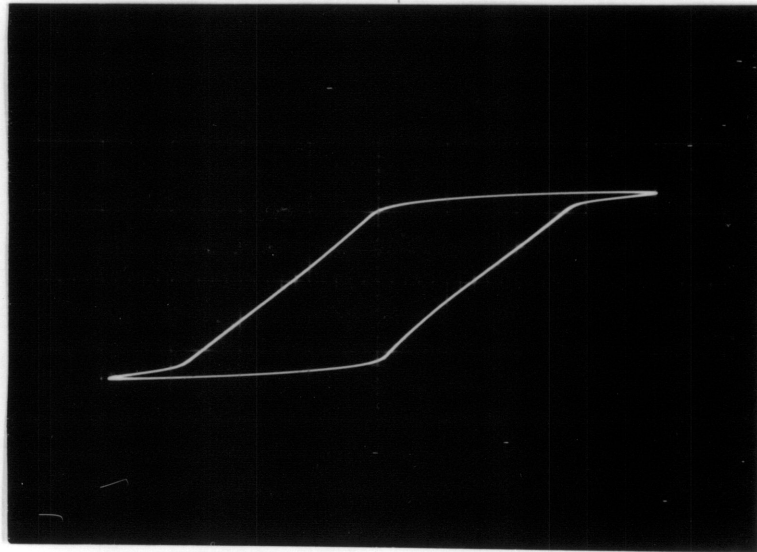
Figure A3.3 Hysteresis Loop for Cold Rolled Steel

Scales: Horizontal: 2366 At-m^{-1}/div.
Vertical: 1.26 Wb-m^{-2}/div.

APPENDIX B

COOLING SYSTEM DESIGN

The dissipation due to I^2R losses in the primary coil on full load is approximately 25W which could be naturally convected from the coil. However "back heat" convected from the hot disk to the coil is much greater. The cooling system is designed assuming 90% efficiency on full load with 1500W input to include copper and "back heat" losses. The total loss is then 150W or 512 BTU/hr.

For turbulent flow inside a cricular tube the heat transfer co-efficient is given by[13]

$$h_i = \frac{k}{D_i} \, 0.023 \, R_e^{0.8} \, P_r^{0.4}$$

where
$$R_e = \frac{\rho v D_i}{\mu}$$

k is the thermal conductivity of the fluid, ρ is the density, v the velocity, μ the viscosity and P_r the Prandtl number, D_i is the inside diameter.

For a velocity flow rate of 6 ft/s and the dimensions of the tube given in Figure 4.1(a) and the properties of water at 140°F* we obtain

$$R_e = 10,672; \quad h_i = 2300 \text{ BTU/ft}^2 \text{ hr°F.}$$

The mass flow rate is

$$\dot{m} = \rho v \, \frac{\pi}{4} \, D_i^2 = 112.3 \text{ lb}_m/\text{hr}$$

---

*Water at 140°F (60°C)[13]; $\rho = 61 \text{ lb}_m/\text{ft}^3$; $C_p = 1 \text{ BTU/lb}_m°F$; K = 0.38 BTU/hr ft°F; $\mu = 1.286 \text{ lb}_m/\text{hr ft}$; $P_r = 3.46$.

The log mean temperature difference is found from

$$\dot{Q} = h_i A_h \Delta T_{\ell m}$$

$$A_h = \pi D_i L$$

$\dot{Q}$ = 512 BTU/hr. A_h is the area for heat transfer found from the coil dimensions, L is the coil length. Thus gives

$$\Delta T_{\ell m} = 0.18°F$$

So essentially the coil wall temperature is at the fluid temperature.

The temperature rise between inlet and outlet is derived from

$$\dot{Q} = \dot{m} C_p \Delta T_L$$

which implies ΔT_L = 4.6°F.

During the experiments this temperature rise was 4.5°F at full load. In the boiling test the rise was smaller since the disk temperature never exceeded the boiling temperature of water 212°F.

The friction factor in the tube is

$$f = \frac{0.0791}{R_e^{0.25}} = 0.0078$$

The pressure drop due to friction is now

$$\Delta P = 4f \frac{L}{D_i} \frac{\rho v^2}{2g_c}$$

g_c = 32.17 lb_m - ft/s^2 lb_f. This gives

$$\Delta P = 26.2 \text{ psi}$$

During the experiments cooling achieved by connecting the coil to the main supply with the flow regulated to 6 ft/s. To form a closed

system a heat exchanger would be necessary. The design of such an exchanger is included.

The dimensions of the heat exchanger surface are shown in Figure B.1. For natural convection with vertical fins the heat transfer co-efficient on the outside is estimated to be h_o = 2 BTU/ft^2 hr°F from manufacturer's data for the Wakefield 489 finned surface.

The fin efficiency is[13]

$$\eta = \frac{\tanh BL}{BL}$$

$$B = \sqrt{\frac{h_o P}{k_f s}}$$

with the parameters defined in Figure B.1.

The flow inside the exchanger is laminar so the heat transfer co-efficient on the inside is

$$h_{fi} = 8.33 \frac{k}{D_e}$$

where D_e = 2W (Figure B.1).

The overall efficiency of the finned exchanger is

$$\varepsilon = \eta \frac{A_f}{A} + \frac{A_u}{A}$$

The overall heat transfer co-efficient referred to the inside wall area A is given by

$$\frac{1}{U} = \frac{1}{\varepsilon h_o} + \frac{d}{k_f} \frac{A}{A_w} + \frac{A}{h_{fi} A_w}$$

For a mass flow rate of 112.3 lb$_m$/hr the separation between the walls was chosen W = 0.25" to increase h_{fi}.
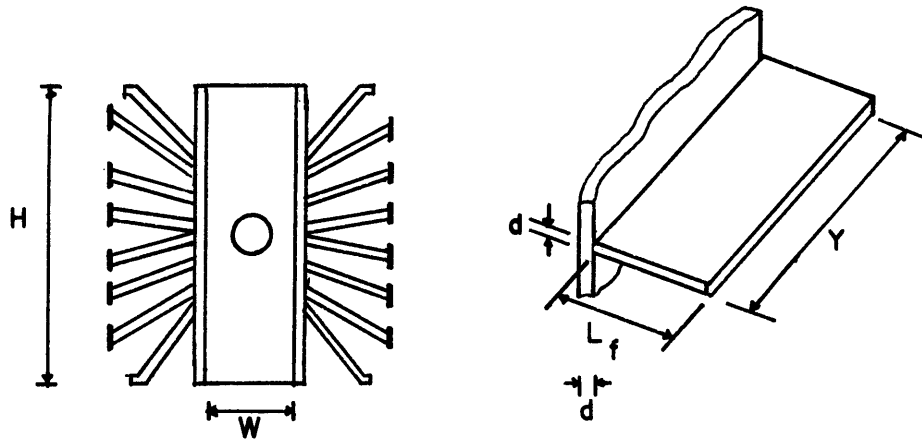
Fin material aluminum k_f = 118 BTU/hr ft °F.

Fins: One Plate (Average)

Number of fins N_f = 9

Fin height   H = 6.25 in.

    width   Y = 9.00 in.

    length L_f = 2.0 in.

    thickness d = 0.08 in.

    perimeter P = 1.5 ft

    cross-
    section   s = 0.72 in^2.

Finned surface
 area (all fins)A_f = 2.25 ft^2

Unfinned surface
 area A_u = 0.34 ft^2

Total heat
 transfer area A = 2.60 ft^2

Plate wall area A_w = 0.39 ft^2

Figure B.1 Heat Exchanger Finned Surface

For the dimensions in Figure B.1 we obtain

$$B = 2.25; \quad \eta = 0.95; \quad \varepsilon = 0.95; \quad R_e = 60;$$

$$h_{fi} = 72 \text{ BTU/ft}^2\text{hr}°\text{F}; \quad U = 1.62 \text{ BTU/ft}^2 \text{ hr}°\text{F}$$

The temperature difference between the fluid and ambient is found from

$$\dot{Q} = 2 \varepsilon \text{ AU } \Delta T_f$$

Where $\dot{Q}$ = 512 BTU/hr as before. A factor of 2 is included to account for finned surfaces at each side of the exchanger.

The fluid mean temperature and consequently the coil wall temperature is now

$$T_w \approx T_f = T_a + 64°\text{F}$$

Where T_a is the ambient temperature. Assuming an ambient temperature of 60°F the coil wall temperature will be 124°F.

The pressure drops due to friction in the exchanger and due to sudden enlargement and contraction at the inlet and outlet of the exchanger are negligible compared with the friction drop in the coil. The pump power is then

$$P = \dot{m} \frac{\Delta P}{\rho} = 8.9 \text{ BTU/hr}$$

APPENDIX C

EXPERIMENTAL AND NUMERICAL DATA

Table C1

Flux Density and Eddy Current Density Distributions

Disk 1: $a_2 = 1.53a$, $z = 2$ cm, $I_m = 30A$ peak $= 21.1A$ rms, $f = 10$ kHz

Theoretical   Experimental

$\frac{r}{a}$	$J_s(A/m^2)$	B_r (Gauss)	B_z (Gauss)	B (Gauss)	μ_r	$\frac{r}{a}$	B (Gauss)
0.18	1.42×10^7	2.24	46.06	46.11	220	0.0	41.0
0.32	2.42×10^7	4.57	46.22	46.45	220	0.2	42.4
0.46	3.61×10^7	8.18	48.18	48.87	221	0.4	45.3
0.60	4.93×10^7	14.36	51.41	53.38	223	0.6	47.4
0.75	6.40×10^7	26.36	52.70	58.93	225	0.8	50.9
0.89	7.78×10^7	47.41	37.53	60.46	226	1.0	35.4
1.03	8.06×10^7	55.08	0.61	55.08	224	1.2	21.2
1.17	6.83×10^7	32.18	13.84	35.03	215	1.4	7.1
1.32	5.41×10^7	15.61	12.35	19.90	209	1.5	4.2
1.46	4.30×10^7	8.14	9.15	12.25	205		
1.53	3.87×10^7	6.10	7.82	9.92	204		

Table C2

Disk Equivalent Current and Resistance as a Function
of Primary Coil Current

Disk 1: a_2 = 1.53a, z = 2cm, f = 10 kHz

I_m(A peak)	I_p(A rms)	R_D(mΩ)	I_{eq}(A)	P_D(W)
5	5.1	5.57	73.6	30
10	10.2	5.61	146.0	120
15	15.2	5.65	217.3	267
20	20.2	5.70	287.6	471
25	25.1	5.74	356.8	731
30	30.0	5.78	425.1	1046
35	34.9	5.83	492.5	1413
40	39.8	5.87	559.0	1834
45	44.6	5.91	624.8	2306
50	49.4	5.95	689.7	2829

Table C3

Coil-Disk Efficiency as a Function of Frequency

The equivalent disk resistance is that corresponding to 1000W disk power at 10 kHz and z = 2cm, the inductive terms also apply for these conditions.

f(kHz)	$X_{\ell}(\Omega)$	$X_m(\Omega)$	$R_D(m\Omega)$	$R_R(\Omega)$	$R_C(\Omega)$	$\eta_{CD}\%$
0.5	0.14	0.14	1.3	0.52	0.020	63.7
1.0	0.27	0.28	1.8	0.72	0.020	82.4
5.0	1.35	1.38	4.1	1.64	0.020	97.1
7.5	2.03	2.06	5.0	2.00	0.020	98.1
10.0	2.71	2.75	5.78	2.31	0.023	98.3

Table C4

Absorbed Disk Power Data for Disk 1

Disk 1: $a_2 = 1.53a$

Experimental						Theoretical			

(a) $z = 2$ cm, $f = 10$ kHz

P_{in} (W)	V_p(V)	I_p(A)	$\theta°$	P_D (W)	I_m (A peak)	V_p(V)	I_p(A)	$\theta°$	P_D(W)
200	54.4	9.5	73.8	143	5	21.8	5.1	70.8	30
400	76.1	13.8	73.8	288	10	43.3	10.1	70.9	120
600	93.1	17.0	73.8	433	15	65.1	15.2	70.9	267
800	108.3	20.0	73.8	592	20	86.6	20.2	71.0	471
1000	119.9	22.2	73.8	732	25	108.1	25.1	71.0	731
1200	125.7	24.1	73.8	831	30	129.5	30.0	71.1	1046
1400	138.5	26.2	73.8	995	35	150.9	34.9	71.1	1413
1600	149.2	28.2	73.8	1155	40	172.3	39.8	71.2	1834
1700	155.2	29.2	73.8	1244					
1900	158.0	29.5	73.8	1280					

(b) $z = 2.5$ cm, $f = 10$ kHz

P_{in} (W)	V_p(V)	I_p(A)	$\theta°$	P_D (W)	I_m (A peak)	V_p(V)	I_p(A)	$\theta°$	P_D(W)
200	58.0	10.2	73.8	163	5	21.7	4.9	73.2	25
400	80.0	14.7	73.8	322	10	43.4	9.7	73.2	97
600	97.5	18.1	73.8	485	15	65.0	14.6	73.3	220
800	112.3	21.1	73.8	650	20	86.5	19.4	73.3	389
1000	126.3	23.7	73.8	822	25	108.0	24.1	73.4	605
1200	135.5	26.5	73.8	985	30	129.5	28.9	73.4	866
1400	147.2	28.8	73.8	1161	35	150.9	33.6	73.4	1171
1600	158.0	30.9	73.8	1336	40	172.2	38.3	73.5	1521

(c) z = 3.0 cm, f = 10 kHz

200	60.3	11.0	73.8	182	5	21.8	4.7	76.2	21
400	84.4	16.0	73.8	368	10	43.4	9.4	76.3	82
600	102.7	19.6	73.8	552	15	65.3	14.0	76.3	183
800	119.1	22.8	73.8	745	20	87.0	18.6	76.3	323
1000	134.3	25.6	75.6	840	25	108.6	23.2	76.4	502
1200	147.7	28.6	75.6	1031	30	130.1	27.8	76.4	720
1400	160.6	31.2	76.5	1144	35	151.6	32.4	76.4	975
1600	173.0	33.5	76.5	1327	40	173.1	36.9	76.5	1267

(d) z = 3.5 cm, f = 10 kHz

200	65.6	12.1	75.6	194	5	22.0	4.5	79.6	17
400	91.6	17.3	75.6	387	10	43.9	9.0	79.6	68
600	111.9	21.4	75.6	584	15	65.8	13.5	79.6	152
800	129.9	25.0	75.6	791	20	87.6	18.0	79.7	269
1000	145.5	28.1	75.6	996	25	109.4	22.5	79.7	419
1200	156.6	31.1	75.6	1187	30	131.2	26.9	79.7	600
1400	170.0	33.6	75.6	1393	35	152.9	31.3	79.7	814
1500	176.0	34.8	75.6	1491	40	174.5	35.7	79.7	1058
					45	191.1	40.1	79.8	1333

(e) z = 4 cm, f = 10 kHz

200	68.8	12.2	77.4	180	5	22.0	4.4	81.9	14
400	96.3	17.5	77.4	360	10	43.9	8.8	81.9	57
600	118.1	21.7	77.4	547	20	87.5	17.4	81.9	225
800	136.6	25.3	77.4	737	30	131.1	26.1	82.0	503
1000	153.0	28.4	77.4	927	40	174.4	34.7	82.0	887

(f) z = 2 cm, f = 7.5 kHz R_C = 0.025Ω

100	34.6	7.7	76.95	60	5	15.9	4.8	71.7	20
200	47.9	11.0	76.95	117	10	31.7	9.5	71.8	78
300	57.8	13.6	76.95	175	15	47.5	14.2	71.8	174
400	65.9	15.8	76.95	230	20	63.3	18.8	71.9	306
500	73.8	17.6	76.95	286	25	79.0	23.5	71.9	475
600	82.1	19.5	76.95	351	30	94.7	28.1	72.0	679

(g) z = 2 cm, f = 15 kHz R_C = 0.03Ω

200	64.4	7.7	72.9	144	5	34.3	5.7	70.2	55
400	88.9	11.2	72.9	289	10	68.5	11.4	70.2	220
600	107.5	13.9	72.9	435	15	102.5	17.0	70.2	491
800	123.8	16.2	72.9	584	20	136.3	22.6	70.2	866
1000	139.2	18.3	72.4	739	25	170.1	28.1	70.2	1343

(h) z = 2 cm, f = 20 kHz R_C = 0.036Ω

200	69.3	6.5	73.8	124	5	49.7	6.3	70.1	85
400	96.1	9.4	73.8	249	10	95.5	12.5	70.1	338
600	117.5	11.8	73.8	384	15	142.8	18.7	70.1	755
800	135.5	13.8	73.8	515	20	189.9	24.9	70.1	1333
1000	151.5	15.5	73.8	646					
1200	167.5	17.1	73.8	789					
1400	182.5	18.5	73.8	932					
1500	189.9	19.3	73.8	1011					

Table C5

Absorbed Disk Power Data for Disk 2

Disk 2: $a_2 = 1.2a$

Experimental						Theoretical			

(a) z = 2 cm, f = 10 kHz

P_{in} (W)	$V_p(V)$	$I_p(A)$	$\theta°$	P_D (W)	I_m (A peak)	$V_p(V)$	$I_p(A)$	$\theta°$	$P_D(W)$
200	57.3	11.0	75.6	153	5	20.9	4.5	73.4	22
400	79.2	15.5	75.6	300	10	41.7	9.0	73.5	86
600	97.4	19.3	75.6	457	15	62.5	13.5	73.6	192
800	116.2	22.5	75.6	637	20	83.3	17.9	73.7	339
1000	131.5	25.4	75.6	813	25	104.0	22.3	73.7	525
1200	140.9	27.4	75.6	943	30	124.6	26.7	73.8	749
1400	152.3	29.7	75.6	1103	35	145.2	31.0	73.9	1012
1600	164.6	32.0	75.6	1286	40	165.8	35.4	73.9	1311
1700	171.0	33.1	75.6	1380	45	186.3	39.7	74.0	1646

(b) z = 2.5 cm, f = 10 kHz

P_{in} (W)	$V_p(V)$	$I_p(A)$	$\theta°$	P_D (W)	I_m (A peak)	$V_p(V)$	$I_p(A)$	$\theta°$	$P_D(W)$
200	63.0	11.9	75.6	183	5	20.8	4.4	75.6	17
400	88.1	17.0	75.6	365	10	41.6	8.7	75.7	69
600	108.4	21.0	75.6	554	15	62.3	13.0	75.8	154
800	126.3	24.4	75.6	751	20	83.0	17.3	75.8	272
1000	142.2	27.4	76.5	892	25	103.7	21.6	75.9	422
1200	152.3	29.8	76.5	1037	30	124.3	25.9	75.9	604
1400	165.0	32.3	77.4	1135	35	144.7	30.1	76.0	816
1600	178.0	34.7	77.4	1320	40	165.4	34.3	76.0	1059

(c) z = 3.0 cm, f = 10 kHz

200	66.6	12.8	77.4	181	5	20.9	4.2	78.4	14
400	92.8	18.1	77.4	359	10	41.7	8.5	78.5	56
600	113.5	22.4	77.4	542	15	62.4	12.7	78.5	125
800	131.9	26.0	77.4	733	20	83.2	16.8	78.6	221
1000	150.0	29.3	78.3	870	25	103.9	21.0	78.6	343
1200	163.4	32.3	78.3	1044	30	124.6	25.2	78.7	490
1400	178.2	34.9	78.3	1230	35	145.2	29.3	78.7	663
1600	192.0	37.5	78.3	1427	40	165.8	33.4	78.8	861

(d) z = 3.5 cm, f = 10 kHz

200	72.9	13.3	79.2	177	10	41.9	8.2	81.6	46
400	102.3	18.9	79.2	354	20	83.6	16.4	81.6	180
600	125.3	23.4	79.2	535	25	104.4	20.5	81.7	280
800	144.6	27.1	79.2	717	30	125.1	24.5	81.7	400
1000	162.7	30.4	79.2	905	35	145.9	28.6	81.7	542
1200	175.0	33.6	79.2	1075	40	166.6	32.6	81.7	704
1400	190.0	37.0	79.2	1285	45	187.3	36.7	81.8	886
1500	197.7	38.5	79.2	1390	50	207.9	40.7	81.8	1088

(e) z = 4.0 cm, f = 10 kHz

200	76.0	13.9	79.2	193	10	41.8	8.0	83.6	37
400	106.0	19.7	79.2	381	20	83.4	16.1	83.7	147
600	130.0	24.3	79.2	578	30	125.0	24.0	83.7	329
800	150.9	28.2	79.2	780	40	166.4	32.0	83.7	578
1000	170.0	31.8	79.2	988	45	187.0	35.9	83.8	729

Table C6

Disk Power as a Function of Coil-Disk Separation

Disk 1: a_2 = 1.53a, I_p = 30A rms, f = 10 kHz

z(cm)	P_D(W) expt.	P_D(W) theor.
2.0	1320	1046
2.5	1261	937
3.0	1092	842
3.5	1116	750
4.0	1020	680

Table C7

Disk Power as a Function of Frequency

Disk 1: a_2 = 1.53a, z = 2cm, I_p = 20A rms

f (kHz)	P_D(W) expt.	P_D(W) theor.
7.5	360	350
10.0	592	465
15.0	890	700
20.0	1060	880

Table C8

Boiling Test Data

2 liter, z = 2cm (induction range)

t(min.)	T(Induction, 1500W)°C	T(Conventional)°C 1500W	1100W
0	20.0	21.0	23.0
1	-	23.0	25.0
2	34.0	29.0	29.5
4	47.5	44.0	40.0
6	60.0	58.5	51.0
8	-	72.0	61.5
9	75.5	-	-
10	79.8	83.5	71.5
12	87.0	91.0	79.0
14	91.0	95.0	85.0
16	-	-	88.0
18	-	-	90.0
22	94.5	-	91.0

Table C9

Test Results for Normalized Magnetization
and Incremental Permeability Curves

$V_{max}(V)$	$I_{max}(A)$	$B_{max}(Wb/m^2)$	$H_{max}(At/m)$	μ_r
0.1	0.040	0.063	118.7	424
0.2	0.065	0.126	192.2	522
0.4	0.096	0.252	284.0	707
0.6	0.132	0.378	390.0	770
0.8	0.182	0.504	538.4	745
1.2	0.320	0.756	946.6	636
1.4	0.540	0.882	1597.0	439
2.0	1.240	1.260	3667.0	273
2.4	1.600	1.512	4732.0	254
2.6	3.000	1.638	8874.0	147
2.8	4.200	1.764	12424.0	113

Table C10

Test Results for Disk Conductivity

The test was made on a bar of uniform cross-section with the following dimensions:

length ℓ = 56.5cm; cross-section A_b = 0.485cm^2;

resistance R = 1.734x10$^{-3}\Omega$; conductivity σ = 6.7x10$^6(\Omega m)^{-1}$

V(mV)	I(A)	R(mΩ)
1.70	1.0	1.700
3.45	2.0	1.725
5.21	3.0	1.737
6.98	4.0	1.745
8.74	8.0	1.748
10.50	6.0	1.750

APPENDIX D

COMPUTER ANALYSIS

In Chapter 3 numerical expressions were derived for the trans-
former model parameters and terminal variables. The attached computer
program is used to evaluate these expressions.

The geometric dimensions of the coil and disk of Figure 4.1 are
read in and also N points on the normalized permeability curve Figure
4.5. The following subprograms are set up to evaluate repeated
calculations.

BINT1 and BINT2 evaluate BI1 and BI2 of equations (3.2.3) and
(3.2.4) respectively.

HENRYL and HENRYM evaluate the self and mutual inductances of
equations (3.214) and (3.2.10) respectively.

HENRYT is a refinement on HENRYM. Strictly speaking the mutual
inductance formula is correct for filaments only and in order to take
finite cross-sections into account Rayleigh's formula[8] is used. With
The central filament, four other filaments are chosen on each edge of
the coil cross-section as shown in Figure D1.1.

The mutual inductance is then

$$M = \frac{1}{6} (M_1 + M_2 + M_3 + M_4 + M_5 + M_6 + M_7 + M_8 - 2M_0) \tag{D1.1}$$

and each M_i is the mutual inductance between the filament at i and the
center filament of the other coil. M_i is evaluated with HENRYM.

SUBROUTINE LAGR interpolates the incremental permeability for a
given flux density from the supplied data points on the magnetization
curve. The Lagrangian Interpolation Formula is used.
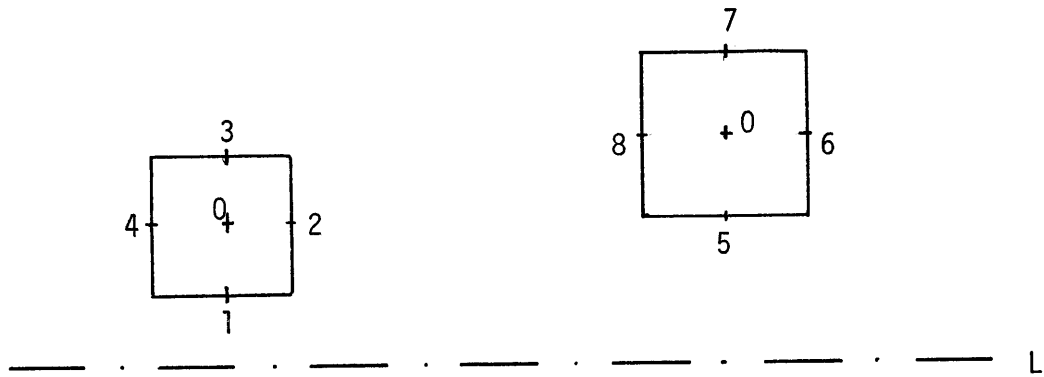
Figure D.1   Rayleigh's Formula for Mutual Inductance

$$y = \sum_{i=k}^{K+m-1} y_i \prod_{\substack{j=k \\ j \neq i}}^{K+m-1} \left(\frac{x - x_j}{x_i - x_j}\right) \qquad (D1.2)$$

An mth degree polynomial is passed through $(m+1)$ points to the left and right of x, the point at which y is being interpolated.

The Trapezoid Rule is used to carry out integration in the equivalent current and power formula, equations (3.2.11) and (3.2.12) respectively.

$$\int_a^b f(x)dx \simeq \frac{h}{2} [f(a) + 2f(a+h) + 2f(a+2h) + 2f(a+(n-1)h) + f(b)] \qquad (D1.3)$$

$$h = \frac{b-a}{n} \qquad (D1.4)$$

where n is the number of trapezoids. In the program the number of trapezoids is equal to the number of disk segments for convenience. It was found that 20 segments gave sufficient accuracy to two decimal places.

SUBROUTINE RMINV inverts a real matrix by the standard Gauss-Jordon Method.

The peak magnetizing current is specified and for a given coil-disk separation the transformer model parameters and terminals variables are

calculated. The flux density and eddy-current density distributions are also printed.

```
C      A=PRIMARY COIL RADIUS
C      B1=PRIMARY COIL WIDTH
C      C1=PRIMARY COIL HEIGHT
C      T=PRIMARY COIL TURNS
C      S=MAGNETISATION CURRENT(PEAK)
C      Z=COIL-DISK SEPARATION
C      M=NO. OF DISK SEGMENTS
C      HZ=FREQUENCY
C      SIGMA=DISK CONDUCTIVITY
C      N=NO. PCINTS ON B-UR CURVE
C      SD=SKIN DEPTH
C      RCAC=A.C. PRIMARY RESISTANCE
C      INDUCTANCE IN MICROHENRIES
C      ALL LENGTHS IN CMS.
C
C      EQUIVALENT RESISTANCE CALCULATION
       REAL*4 B(10),U(10),BR(20),BZ(20),BC(20),UC(20),SJ(20),FX1(20),FX2(
      120),S
       COMPLEX SP,VP,CMPLX,Z1,Z2,Z3,Z4,Z5
       EXTERNAL HENRYM
       REAL*4 L1,LL,LM,L(20,20),M1(20),P(20),C(20)
       INTEGER*4 IWORK(20,2),IERR
       INTEGER*4 KK,II
       READ(5,1) N,M,A,Z,T,HZ,SIGMA,(B(J),U(J),J=1,N)
       READ(5,10) C1,B1
     1 FORMAT(2I3/4F10.4,E10.2/(8F10.4))
     2 FORMAT(' ',6E14.4)
    10 FORMAT(2F10.4)
       A1=0.175*A
       A2=1.53*A
       DR=(A2-A1)/(M-1.)
       DO 18 KK=4,8
       Z=KK/2.
       DO 18 II=5,50,5
       S=II
       G=2.*3.1416E-09*T*S*A
```

```
      D=2.*3.1416*HZ*SIGMA*G
      DO 12 J=1,M
      P(J)=A1+(J-1.)*DR
      R=P(J)
      BR(J)=G*BINT2(R,A,Z)*1.E 04
      BZ(J)=G*ABS((R+DR)*BINT1(R+DR,A,Z)-R*BINT1(R,A,Z))/R/DR*1.E 04
      BC(J)=SQRT(BR(J)**2+BZ(J)**2)
      SJ(J)=D*BINT1(R,A,Z)*1.E 04
C
C     LAGRANGIAN INTERPOLATION
      CALL LAGR(B,U,BC(J),UC(J),N,5,K)
   12 CONTINUE
      AMPS=0.
      WATTS=0.
      DO 13 J=1,M
      FX1(J)=SJ(J)**2/SQRT(39.478E-9*HZ*SIGMA*UC(J))*P(J)/2.
      FX2(J)=SJ(J)/SQRT(39.478E-09*HZ*SIGMA*UC(J))/2.
      WATTS=WATTS+FX1(J)
      AMPS=AMPS+FX2(J)
   13 CONTINUE
      AMPS=(2.*AMPS-FX2(1)-FX2(M))*DR/2.*1.E-04
      WATTS=(2.*WATTS-FX1(1)-FX1(M))*DR/2.*1.E-08*3.1416/SIGMA
      OHMS=WATTS/AMPS**2
      IF(S.NE.30.) GO TO 25
      PRINT 14
   14 FORMAT(' ','     RADIUS R        BR(R)           BZ(R)             BC(R)
     1         UR(R)           JS(R)')
      PRINT 2,(P(J),BR(J),BZ(J),BC(J),UC(J),SJ(J),J=1,M)
   25 PRINT 15
   15 FORMAT(' ','     I EQ.(A)        PD(W)           RD(OHMS)          IM(PEAK)
     1         RADIUS A        Z(CM)')
      PRINT 2,AMPS,WATTS,OHMS,S,A,Z
C
      IF(S.GT.6.) GO TO 20
C     EQUIVALENT INDUCTANCE CALCULATIONS
      EZ=DR
```

```
      C2=1./SQRT(39.478E-09*HZ*SIGMA*UC(M))
      L1=HENRYL(A,C1,B1)
      DO 5 I=1,M
      L(I,I)=HENRYL(P(I),C2,B2)
      K=I+1
      IF(K.GT.M) GO TO 5
      DO 4 J=K,M
      L(I,J)=HENRYM(P(I),P(J),0.)
    4 L(J,I)=L(I,J)
    5 M1(I)=HENRYT(A,P(I),B1,C1,B2,C2,Z)
      CALL RMINV(20,M,L,DETERM,IWORK,IERR)
      DO 6 I=1,M
      C(I)=0.
      DO 6 K=1,M
    6 C(I)=C(I)+L(I,K)*M1(K)
      C3=0.
      DO 7 I=1,M
    7 C3=C3+M1(I)*C(I)
      LL=L1-C3
      L1=L1*(T**2)
      LL=LL*(T**2)
      LM=C3*(T**2)
      PRINT 16
   16 FORMAT(' ','      LS              LL              LM              SD
     1        SEPARATION      FREQUENCY')
      PRINT 2,L1,LL,LM,C2,Z,HZ
C
C     TERMINAL VARIABLES CALCULATIONS
   20 SD=C2
      RCAC=2.32E-04*SQRT(HZ)
      SRMS=S/SQRT(2.)
      AMPSP=AMPS/T
      XLM=2.*3.142*HZ*LM*1.E-06
      XLL=2.*3.142*HZ*LL*1.E-06
      EP=XLM*SRMS
      Z1=CMPLX(SRMS,0.)
```

```
      Z2=CMPLX(0.,AMPSP)
      Z3=CMPLX(0.,EP)
      Z4=CMPLX(0.,XLL)
      Z5=CMPLX(RCAC,0.)
      SP=Z1+Z2
      CP=CABS(SP)
      VP=Z3+Z5*SP+Z4*SP
      PRINT 17
   17 FORMAT(' ','      VP: REAL    , IMAGINARY     IP: REAL    , IMAGINA
     1RY     IM(RMS)        CP')
      PRINT 2,VP,SP,SRMS,CP
      AVP=ATAN(AIMAG(VP)/REAL(VP))
      ASP=ATAN(AIMAG(SP)/REAL(SP))
      THETA=(AVP-ASP)*180./3.14159+180.
      VPM=CABS(VP)
      PRINT 19,THETA,VPM ,CP
   19 FORMAT(' ','THETA=',F10.4,'VPM=',F10.4,'CP=',F10.4)
   18 CONTINUE
    9 PRINT 17
      STOP
      END
      FUNCTION HENRYL(A,C,B)
      R=0.2235*(B+C)
      HENRYL=0.01256637*A*(ALOG(8.*A/R)*(1.+(3./16.)*((R/A)**2))-(2.+((R
     1/A)**2)/16.))
      RETURN
      END
      FUNCTION HENRYM(A1,A2,S)
      C=((A1-A2)**2+S**2)/(16.*A1*A2)
      HENRYM=0.01256637*SQRT(A1*A2)*(ALOG(2./SQRT(C))*(1.+3.*C-3.75*(C**
     12))-(2.+C-3.875*(C**2)))
      RETURN
      END
      FUNCTION HENRYT(A1,A2,B1,C1,B2,C2,S)
      REAL*4 M(8),MO
      MC=HENRYM(A1,A2,S)
```

```
      M(1)=HENRYM(A1-C1/2.,A2,S)
      M(2)=HENRYM(A1,A2,S-B1/2.)
      M(3)=HENRYM(A1+C1/2.,A2,S)
      M(4)=HENRYM(A1,A2,S+B1/2.)
      M(5)=HENRYM(A1,A2-C2/2.,S)
      M(6)=HENRYM(A1,A2,S+E2/2.)
      M(7)=HENRYM(A1,A2+C2/2.,S)
      M(8)=HENRYM(A1,A2,S-E2/2.)
      HENRYT=0.
      DO 1 I=1,8
    1 HENRYT=HENRYT+M(I)
      HENRYT=(HENRYT-MO*2.)/6.
      RETURN
      END
      FUNCTION BINT1(R,A,Z)
      C=((A-R)**2+Z**2)/(16.*A*R)
      BINT1=((1.+3.*C-3.75*C**2+8.75*C**3)*ALOG(2./SQRT(C))-(2.+C-3.875*
     1C**2+10.292*C**3))/(3.1416*SQRT(A*R))
      RETURN
      END
      FUNCTION EINT2(R,A,Z)
      C=((A-R)**2+Z**2)/(16.*A*R)
      BINT2=Z*((-3.+7.5*C-26.25*C**2)*ALOG(2./SQRT(C))+(1./(2.*C)+2.5-9.
     1625*C+35.25*C**2))/(8.*3.1416*((A*R)**1.5))
      RETURN
      END
      SUBROUTINE LAGR(XC,YC,X,Y,N,M1,J)
      REAL*4 XC(10),YC(10)
      IF(X-XC(1)) 1,2,2
    1 J=1
      Y=0.
      RETURN
    2 IF(X-XC(N)) 3,3,1
    3 J=0
      DO 4 M=2,N
      IF(XC(M)-X) 4,5,5
```

```
      4 CONTINUE
      5 JE=M+M1/2
        JS=JE-M1
        IF(JS) 6,6,7
      6 JS=1
        JE=1+M1
        GO TO 8
      7 IF(JE-N) 8,8,9
      9 JE=N
        JS=JE-M1
      8 Y=0.
        DO 10 I=JS,JE
        SUM=1.
        DO 11 J=JS,JE
        IF(J-I) 12,11,12
     12 SUM=SUM*(X-XC(J))/(XC(I)-XC(J))
     11 CONTINUE
     10 Y=Y+SUM*YC(I)
        RETURN
        END
C
C      DATA
C N SEGMENTS
  10 20
C RADIUS    SEPARATION  TURNS    FREQUENCY  CONDUCTIVITY
9.0         2.0         20.       10000.     6.7E 04
C FLUX DENSITY(WB/M SQ.)    RELATIVE PERMEABILITY
0.          200.        0.05      370.       0.1        470.       0.15       542.
0.2         610.        0.3       700.       0.4        745.       0.5        740.
0.6         720.        0.7       670.
C HEIGHT   WIDTH
1.0        5.5
```

BIBLIOGRAPHY

1.   Moreland II, W.C., "The Induction Range: Its Performance and Development Problems", IEEE Transactions on Industry Applications, Vol. IA-9, Jan./Feb. 1973.

2.   Mennie, D., "Microwave Ovens: Whats Cooking?", IEEE Spectrum, March 1975.

3.   Peters, P.H., "A Portable Cool-Surface Induction Cooking Appliance", IEEE Transactions on Industry Applications, Vol. IA-10, Nov./Dec. 1974.

4.   Woodson, H.H. and Melcher, J.R., "Electromechanical Dynamics", J. Wiley and Sons, Inc., New York 1968, Chapter 1, part I.

5.   Panofsky, K.A. and Phillips, M., "Classical Electricity and Magnetism", Addison-Wesley, Reading, Mass., 1962, Chapters 8 and 10.

6.   Morse, P. and Feshback, H., "Methods of Theoretical Physics", McGraw-Hill, New York, 1953, Chapter 6, Part I.

7.   Ryder, J.D., "Networks, Lines and Fields", Prentice-Hall Inc. New York, 1955, p. 337-442.

8.   Bulletin of the Bureau of Standards, Vol. 8, No. 1, Government Printing Office, January 1912, Eqns. 16, 23, 86.

9.   Havelock, T.H., "On Certain Bessel Integrals and the Co-efficients of Mutual Induction of Coaxial Coils", Philosophical Magazine S. 6., Vol. 15, No. 87, March 1908.

10.   Mapham, N., "An SCR Inverter with Good Regulation and Sine-wave Output", IEEE Transactions on Industry and General Applications, Vol. IGA-3, No. 2, Mar./Apr. 1967.

11.   Wu, S.J., "Analysis and Design of Optimized Snubber Circuits for dV/dt Protection in Power Thyristor Applications", IEEE IGA 1970 Annual Meeting, Chicago, Illinois, October 1970.

12.   Roberge, J.K., "Operational Amplifiers, Theory and Practice", J. Wiley and Sons, Inc., New York, 1975, Chapter 1.

13.   Rohsenow, W.M. and Choi, Y., "Heat Mass and Momentum Transfer", Prentice-Hall, Inc., New York, 1961, Chapters 4, 6 and Appendix E.